Impact of ENSO on the Variability of the Asian–Australian Monsoons as Simulated in GCM Experiments

NGAR-CHEUNG LAU AND MARY JO NATH

NOAA/Geophysical Fluid Dynamics Laboratory, Princeton University, Princeton, New Jersey

(Manuscript received 10 August 1999, in final form 4 February 2000)

ABSTRACT

The influences of El Niño–Southern Oscillation (ENSO) on the summer- and wintertime precipitation and circulation over the principal monsoon regions of Asia and Australia have been studied using a suite of 46-yr experiments with a 30-wavenumber, 14-level general circulation model. Observed monthly varying sea surface temperature (SST) anomalies for the 1950–95 period have been prescribed in the tropical Pacific in these experiments. The lower boundary conditions at maritime sites outside the tropical Pacific are either set to climatological values [in the Tropical Ocean Global Atmosphere (TOGA) runs], predicted using a simple 50-m oceanic mixed layer (TOGA-ML runs), or prescribed using observed monthly SST variations. Four independent integrations have been conducted for each of these three forcing scenarios.

The essential characteristics of the model climatology for the Asian–Australian sector compare well with the observations. Composites of the simulated precipitation data over the outstanding warm and cold ENSO events reveal that a majority of the warm episodes are accompanied by below-normal summer rainfall in India and northern Australia, and above-normal winter rainfall in southeast Asia. The polarity of these anomalies is reversed in the cold events. These relationships are particularly evident in the TOGA experiment.

Composite charts of the simulated flow patterns at 850 and 200 mb indicate that the above-mentioned precipitation changes are associated with well-defined circulation features over the affected monsoon regions. Dry conditions are typically coincident with low-level anticyclonic anomalies, and vice versa. These circulation centers are situated to the northwest and southwest of a prominent precipitation anomaly situated near 120°–150°E at the equator, which corresponds to the western half of a dipolar heating pattern resulting from east–west displacements of the ascending branch of the Walker circulation during ENSO. The large-scale anomalous circulation over the monsoon regions is similar to that of a Rossby wave pattern associated with a condensational heat source or sink in the western equatorial Pacific.

Diagnosis of the output from the TOGA-ML experiment reveals that variations in the circulation and cloud cover accompanying ENSO-induced monsoon anomalies could modulate the latent heat and shortwave radiative fluxes at the air–sea interface in the Indian Ocean, thereby changing the SST conditions in that basin. These simulated SST anomalies compare well with observational results. The local atmospheric response to these SST anomalies opposes the remote response of the south Asian monsoon flow to SST anomalies in the tropical Pacific, thus leading to a negative feedback loop in the air–sea coupled system.

1. Introduction

The relationships between the Asian–Australian monsoons and El Niño–Southern Oscillation (ENSO) episodes in the tropical Pacific have long been a subject of considerable scientific and practical interest. Empirical studies of such connections date back to the seminal works of Walker (1923, 1924). The potential applications of Southern Oscillation as a tool for predicting the intensity of the Indian summer monsoon were considered by Normand (1953) and Troup (1965), among many others. The association of various ENSO events in the past century with monsoon fluctuations was documented in detail by Angell (1981), Rasmusson and Carpenter (1983), Shukla and Paolino (1983), and Mooley and Parthasarathy (1983) for India; Li (1990), Zhang et al. (1996), and Chang et al. (2000a,b) for the eastern Asian sector; and McBride and Nicholls (1983) and Drosdowsky and Williams (1991) for Australia. A comprehensive description of the ENSO-related precipitation patterns in various parts of the Asian–Australian monsoon region was also given by Ropelewski and Halpert (1987, 1989). The collective evidence presented in these studies indicate that warm ENSO events are often accompanied by below-normal monsoon rains over India and Australia, whereas wet conditions occur during cold events. However, Krishna Kumar et al. (1999) recently noted that the inverse relationship between ENSO and the Indian monsoon has weakened considerably in

Corresponding author address: Dr. Ngar-Cheung Lau, NOAA/Geophysical Fluid Dynamics Laboratory, Princeton University, P.O. Box 308, Princeton, NJ 08542.
E-mail: gl@gfdl.gov

TABLE 1. Survey of modeling studies on the sensitivity of the Asian–Australian monsoon to SST anomalies.

	Model*	Duration of varying SST forcing	Number of model realizations	Domain of varying SST forcing
Palmer et al. (1992)	ECMWF T42L19	JJA 1987 JJA 1988	1	Tropical Pacific Tropical Indian Ocean Tropical Atlantic Extratropics
Kitoh (1992)	MRI 5° × 4°-L5	1969–90	1	Global
Chen and Yen (1994)	NCAR CCM1 R15L12	1975–91	1	Entire Pacific basin
Ju and Slingo (1995)	UGAMP–ECMWF T42L19	1979–88	1	Global
Sperber and Palmer (1996)	32 modeling groups	1979–88	1	Global
	ECMWF T42L19	1979–88	6	Global
	SNG R15L18	1979–88	5	Global
Soman and Slingo (1997)	UGAMP–ECMWF T42L19	1983, 1984, 1994	1	Tropical Pacific
		1979–88	1	Global
Goswami (1998)	GFDL R30L14	1979–93	1	Global
Arpe et al. (1998)	ECHAM3 T42L19	JJA 1987, 1988	3	Tropical Pacific Tropical Indian Ocean Tropical Atlantic
		1979–92	5	Global
		1979–92	1	Tropical Pacific
Lau and Bua (1998)	GEOS 5° × 4°-L13	1980–89	1	Global
Meehl and Arblaster (1998)	NCAR CCM3 T42L18	1950–94	1	Global
Yang and Lau (1998)	GLA 5° × 4°-L17	1979–88	1	Global

* The following acronyms are used for various modeling groups: ECMWF (European Centre for Medium-Range Weather Forecasts); MRI (Meteorological Research Institute); NCAR (National Center for Atmospheric Research), UGAMP (U.K. Universities' Global Atmospheric Modelling Programme); SNG (State University of New York at Albany–NCAR–Genesis); GFDL (Geophysical Fluid Dynamics Laboratory); ECHAM (ECMWF-Max-Planck Institut für Meteorologie in Hamburg); GEOS (Goddard Earth Observing System); and GLA (Goddard Laboratory for Atmospheres). CCM1 and CCM3 stand for various versions of the NCAR Community Climate Model. For spectral models, T42 indicates triangular truncation at 42 wavenumbers; R15 (R30) indicates rhomboidal truncation at 15 (30) wavenumbers. The number of vertical levels is indicated after the letter L.

the past two decades. Li (1990) and Zhang et al. (1996) reported that the strength of the wintertime northeasterly monsoon flow over eastern Asia is typically weaker than normal in warm ENSO events. The scientific issues pertinent to the linkage between the monsoons and ENSO were discussed in the recent review papers by Webster and Yang (1992) and Webster et al. (1998).

The above observational findings have motivated many investigators to conduct modeling studies on the sensitivity of the principal monsoon systems to changes in the conditions of the surface ocean. A majority of such numerical experiments were performed by subjecting atmospheric general circulation models (GCMs) to observed sea surface temperature (SST) anomalies prescribed in various parts of the world oceans. A summary of some of the representative works based on this general methodology is given in Table 1. Thus far, most of the model runs are of rather short duration. Some of these experiments are devoted to specific events, such as the dry and wet Indian monsoons in 1987 and 1988, respectively. Others are concerned with monsoon variability within the 10-yr experimental span (1979–88) of the Atmospheric Model Intercomparison Project (see Gates 1992). In most of the studies listed in Table 1, only a single model run has been performed for a given SST forcing scenario.

The results from the above modeling studies indicate that, among the various oceanic sites being considered, the tropical Pacific exerts the strongest influence on the circulation pattern in the Asian–Australian monsoon region. Generally speaking, simulations of the interannual variability of the broad-scale monsoon flows (e.g., the vertical shear of the zonal wind over the equatorial Indian Ocean) are more realistic than those of regional details (e.g., the local precipitation anomalies over India). Models with better long-term climatologies of the tropical circulation are more successful in reproducing the observed ENSO–monsoon relationships. The experiments performed by some of the modeling groups further indicate that, in addition to SST changes in the tropical Pacific, other processes such as atmosphere–land interactions, extratropical influences, quasi-biennial circulation changes, and internal atmospheric dynamics may also contribute to monsoon variability. These model findings on various alternative mechanisms lend some support to the studies of Barnett et al. (1989), Yasunari (1989), Meehl (1994), and Sankar Rao et al. (1996).

The primary goal of the present investigation is to examine the ENSO–monsoon relationship on the basis of a much more expanded suite of integrations with a GCM that is capable of simulating the monsoon climatology with an acceptable degree of fidelity. Experiments with different SST forcing scenarios are con-

ducted to delineate the relative contributions of SST fluctuations in the tropical Pacific and those in the near-global oceans to monsoon variability, and to investigate the role of air–sea feedback processes. All ENSO events occurring within the 1950–95 period are considered. For each SST scenario, the statistical sampling of the model signals is enhanced by generating four independent realizations of the model response to the same sequence of boundary forcing. Attention is given to summertime as well as wintertime monsoon features on both the planetary and regional scales. A comprehensive approach is taken to document the simulated variability in different subregions of the Asian–Australian monsoon complex, including India, Southeast Asia, and northern Australia. The dynamical basis for the linkage between SST forcing in the tropical Pacific and the monsoons in these regions is critically examined. The potential contributions of local air–sea interactions to monsoon variability is also assessed.

The model experiments and observational data base for this study are described in section 2. The model climatology for the Asian–Australian region is compared with observations in section 3. The simulated and observed precipitation anomalies in this region for selected warm and cold ENSO events are presented in section 4. The composite changes in the three-dimensional circulation pattern in response to the ENSO episodes are considered in section 5. Impact of SST anomalies situated outside the tropical Pacific, as well as local air–sea interactions, on monsoon variability are explored in section 6. A summary and discussion of the principal findings of this study are offered in the concluding section.

2. Experimental design and datasets

The GCM used for this investigation has been developed and maintained by the Climate Dynamics Project at the Geophysical Fluid Dynamics Laboratory (GFDL). A spectral formulation is used to represent the horizontal variations of the model fields, with a rhomboidal truncation at 30 wavenumbers (or R30). The resolution of the corresponding Gaussian grid is 3.75° and ~2.2° in the zonal and meridional directions, respectively. Vertical variations are depicted using a sigma coordinate with 14 levels. A comprehensive set of boundary conditions and physical processes has been incorporated in this model, including ocean–continent contrast, orography, precipitation, predicted cloud cover, radiative transfer, gravity wave drag, ground hydrology, and continental snow cover. The filtering technique introduced by Lindberg and Broccoli (1996) has been applied to the surface topography to reduce spectral truncation errors, thus producing more realistic simulations of the precipitation field. Details of the model numerics have been documented in Gordon and Stern (1982) and Broccoli and Manabe (1992). A climatological atlas of a large variety of fields generated by this model has been compiled by Alexander and Scott (1995).

The model experiments for this study have been conducted by prescribing the temporally varying SST conditions in specific ocean sites as observed in the 46-yr period from January 1950 through December 1995. The gridded analyses of the observed SST field were produced at the National Centers for Environmental Prediction (NCEP) using a reconstruction technique based on empirical orthogonal functions, as described in Smith et al. (1996). Altogether three sets of experiments have been performed, with each set corresponding to a different SST forcing scenario, as follows.

- SST anomalies were inserted in the tropical Pacific between ~25°S and ~25°N only. Climatological (but seasonally varying) values were inserted in all remaining ocean grid points. Such integrations will be referred to as the Tropical Ocean Global Atmosphere (TOGA) runs, and are intended for studying the atmospheric response to SST variability that is directly associated with ENSO events in the tropical Pacific.
- SST anomalies were inserted in the tropical Pacific between ~25°S and ~25°N only. For all remaining ocean grid points that are ice-free throughout the year, the SST conditions were predicted by a simple mixed-layer model, which computes the temperature of a motionless, 50-m slab of water in response to the changing heat fluxes at the air–sea interface. This TOGA-mixed layer (TOGA-ML) simulation considers both the response to SST changes prescribed in the tropical Pacific, and the variability arising from simplified air–sea coupling outside of the tropical Pacific.
- SST anomalies were inserted at all ice-free ocean grid points between ~40°S and ~60°N. Climatological conditions were prescribed at all remaining maritime sites. This set will be called the Global Ocean Global Atmosphere (GOGA) experiment, and delineates the impact of SST conditions in the near-global oceans on atmospheric variability.

For each of the three SST scenarios described above, four parallel integrations initiated from independent atmospheric conditions have been completed. Hence the entire dataset generated by this collection of model runs consists of 3 (forcing scenarios) × 4 (samples) × 46 = 552 yr of integration. The independent conditions used to initiate various integrations were taken from different years of a century-long control run with the same model subjected to climatological SST at all ocean points.

The basic experimental design for this study is almost identical to that used in our previous investigations of

extratropical atmospheric and oceanic variability related to ENSO (Lau and Nath 1994, 1996), with the notable exception that the earlier works were based on a lower-resolution model, with nine vertical levels and truncation at 15 wavenumbers (R15). The R15 integrations were conducted by using a different data source for the observed SST forcing for the 1946–88 epoch. The R30 version of this model is deemed to be a more appropriate tool for examining the ENSO–monsoon relationships, in view of the improved model climatology in the tropical Asian–Australian sector (see section 3) as compared to that simulated in the R15 version (not shown). The R30 model also yields relatively more realistic precipitation and circulation responses in the tropical Pacific to prescribed SST anomalies in that region (see sections 4 and 5).

Prior to this study, Goswami (1998) has considered the impact of SST changes on the summer Indian monsoon by diagnosing an experiment based on the GFDL R30 model and with a design similar to that of GOGA. His experiment consists of a single realization of the model response during the 15-yr period of 1979–93. Hence the present investigation may be viewed as an extension of Goswami's work through lengthening of the time span of the experiments, consideration of a variety of SST forcing scenarios, and performance of multiple runs for each scenario.

Some of the model results reported herein will be compared with the corresponding fields of the observed atmosphere, as obtained from the reanalysis products of NCEP and the National Center for Atmospheric Research (NCAR) for the 1950–97 period (see Kalnay et al. 1996). Estimates of the observed precipitation field for the 1979–96 period are based on the Climate Prediction Center Merged Analysis of Precipitation (CMAP) compiled by Xie and Arkin (1997) using rain gauge reports, satellite measurements and reanalysis data.

3. Climatological fields

We first evaluate the fidelity of the climatological characteristics in the monsoon region as simulated by the R30 model. Shown in Fig. 1 are the long-term averaged distributions of precipitation (panels a and b), near-surface streamlines and isotachs (panels c and d), and 200-mb streamlines and isotachs (panels e and f), for the June–July–August (JJA) season. The corresponding fields for the December–January–February (DJF) season are displayed in Fig. 2. The left panels in each figure are based on averages over the 46-yr integration span for all four runs of the TOGA experiment. Corresponding model climatologies for the TOGA-ML and GOGA experiments (not shown) are very similar to the TOGA results presented here. The right panels are obtained by averaging over the 18-yr period of the CMAP dataset (for the precipitation field) and the 48-yr period of the NCEP–NCAR reanalyses (for the wind fields).

In the northern summer, the mean precipitation pattern for both the model (Fig. 1a) and observed (Fig. 1b) atmospheres exhibits maxima in the Bay of Bengal–Indochina and Philippine Sea regions, whereas dry conditions prevail over Australia. The observed precipitation maximum on the western shore of India is not evident in the simulated pattern. The model climate is excessively wet over the Tibetan Plateau, and is too dry along the equatorial Indian Ocean. A general agreement exists between model and observations with regards to the large-scale circulations near the surface and at 200 mb (Figs. 1c–f). At the lower level, the noteworthy common features include the onshore, southwesterly flow over south Asia and southeasterly flow over eastern Asia, as well as the offshore, southeasterly flow over northern Australia. The southeasterly flow over the southern portion of the Indian Ocean is weaker in the model than in the observed atmosphere. The resulting underestimation of the surface convergence over the equatorial Indian Ocean may be linked to the deficient precipitation simulated in that region. At the upper level, the model and observed patterns are dominated by the Tibetan anticyclone and the intensified easterly airstream on its southern flank. The easterly jet simulated over south Asia is stronger than its observed counterpart. The model anticyclone extends too far toward the subtropical western Pacific.

In the northern winter, the model reproduces the wet conditions over the Indonesian archipelago, northern Australia, and the tropical Indian Ocean (see Figs. 2a,b). The simulated precipitation rates are too high over the Tibetan Plateau, northern India and southern China, and too low over the equatorial Indian Ocean. The surface circulation pattern in both model and observations (Figs. 2c,d) is characterized by offshore, northeasterly flows over the Asian monsoon region, and by convergence over the equatorial Indian Ocean, northern Australia, and the southwestern portion of the tropical Pacific. The most notable feature in the simulated and observed flow fields at 200 mb (Figs. 2e,f) is the pair of anticyclones straddling the equator over the western Pacific.

4. Precipitation anomalies during ENSO events

a. Selection of ENSO events

We shall adopt a composite approach to analyze the typical atmospheric responses for a set of outstanding ENSO episodes within the 1950–95 period. After considering the listings of events compiled by various authors (see the review of Trenberth 1997), we have chosen the eight warm events that occurred in 1957, 1965, 1969, 1972, 1976, 1982, 1987, and 1991, and the eight cold events of 1950, 1954, 1955, 1964, 1970, 1973, 1975, and 1988. In each of these 16 events, the monthly SST anomaly in the 5°S–5°N, 120°–150°W region exceeds the ± 0.4°C threshold for a duration of more than

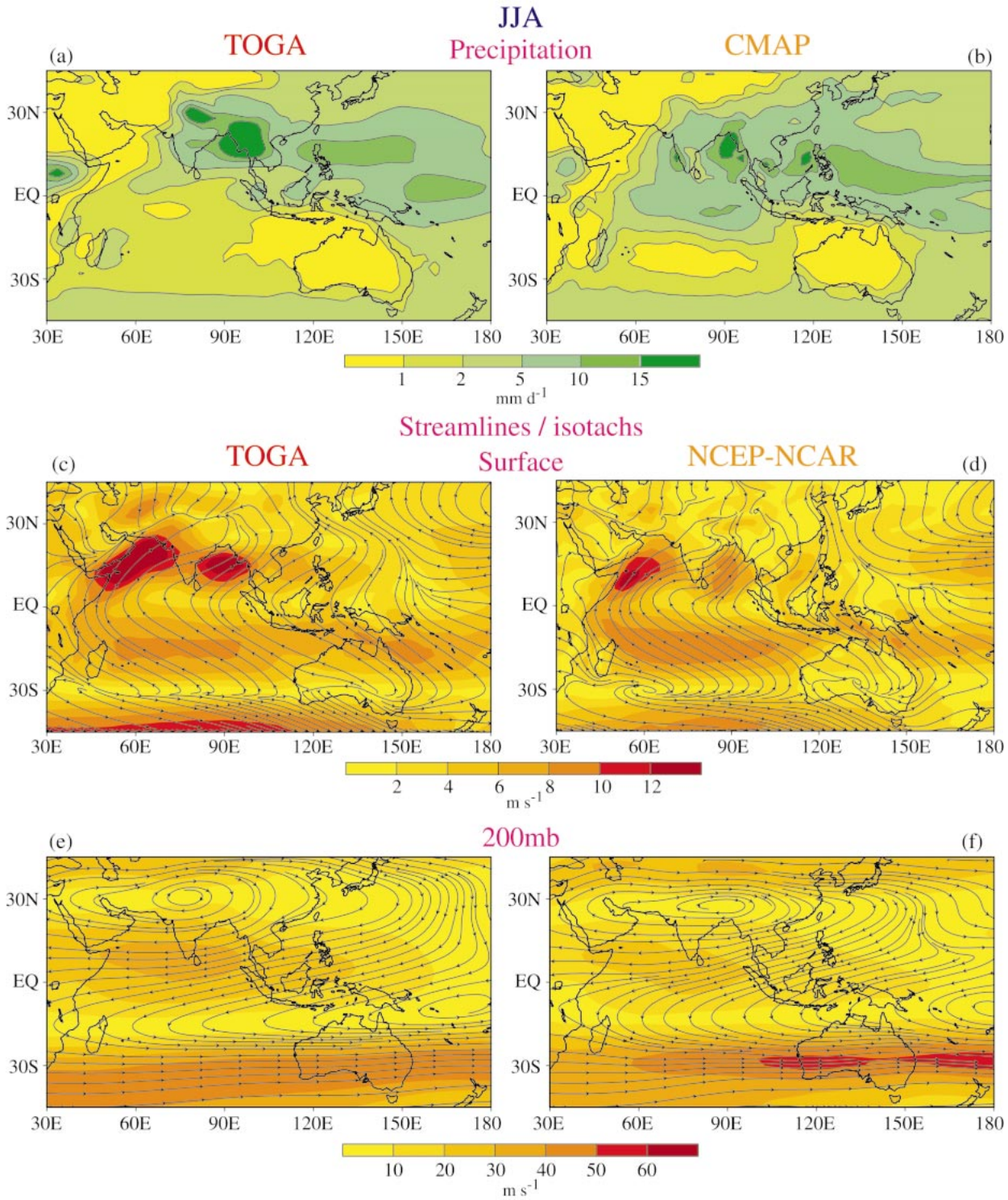

FIG. 1. Climatological distributions of [(a), (b)] precipitation, [(c), (d)] near-surface streamlines and isotachs (shading), and [(e), (f)] 200-mb streamlines and isotachs, for the JJA season. Patterns in the left panels show the ensemble averages of the output from the four TOGA runs. Patterns in the right panels are based on observational estimates of the CMAP dataset (for precipitation) and the NCEP–NCAR reanalyses (for the horizontal wind field at an altitude of 10 m and at the 200-mb pressure level). Note the uneven contour intervals in the precipitation charts. Units for scale bars are mm day^{-1} for precipitation and m s^{-1} for wind speeds.

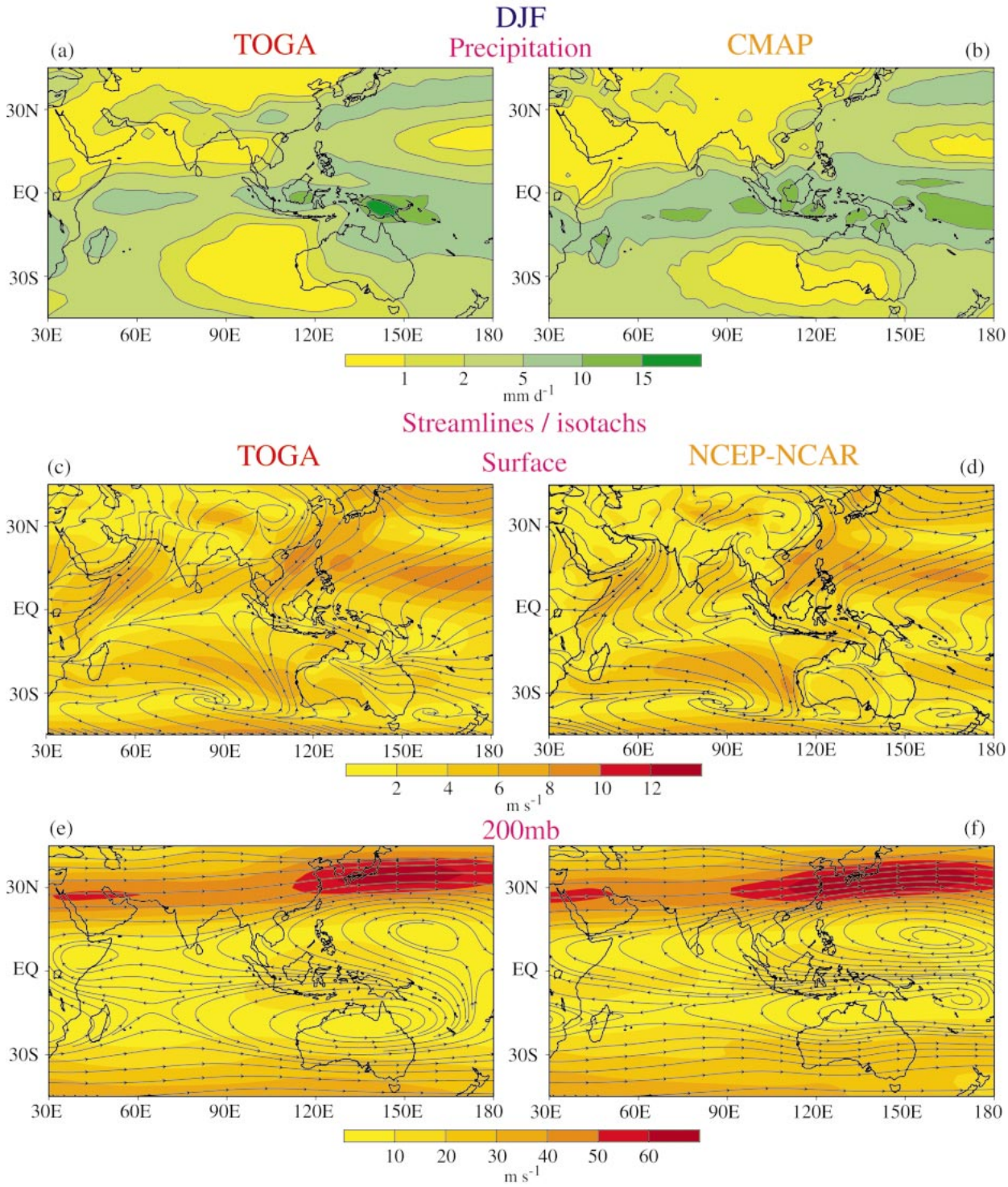

FIG. 2. As in Fig. 1, but for the DJF season.

12 months (see Table 2 of Trenberth 1997). The years corresponding to the selected warm or cold events are designated as year (0). The years preceding and following these events are designated as year (−1) and year (+1), respectively.

b. Composite patterns

For each of the three experiments described in the previous section, the precipitation anomaly (defined as departure from the 46-yr climatology) for a given season

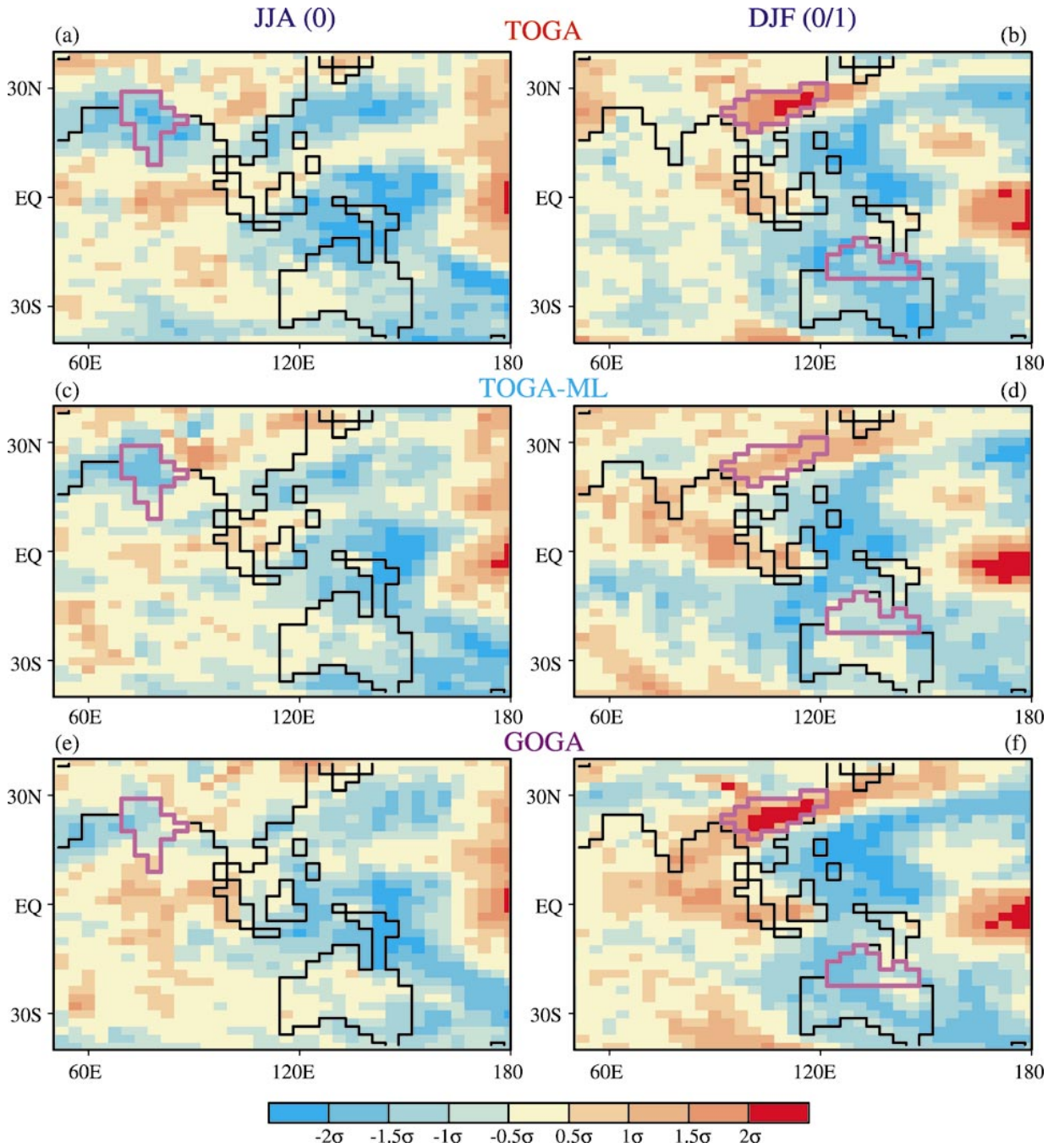

FIG. 3. Distributions of the differences between the composite of precipitation anomalies in eight warm ENSO events and the corresponding composite in eight cold events (referred to as ''warm minus cold composites'' in the text). These charts are based on four-run averages of the [(a),(b)] TOGA, [(c), (d)] TOGA-ML, and [(e), (f)] GOGA experiments, for the (left panels) JJA season of year (0) and (right panels) DJF season of year (0/1). The anomalies at individual model grid boxes have been normalized by the local temporal standard deviation. The purple borders indicate extent of the IND, SEA, and AUS regions, for which area-averaged precipitation indices are to be constructed.

of a given year was averaged over the ensemble of four individual runs. Averages were then taken of these ensemble means over the eight selected warm events to yield the ''warm composites.'' Similarly, the ''cold composites'' were computed by averaging over the eight cold events. The composite data were then normalized by the local standard deviation σ for the respective calendar season. The quantity σ was computed on the basis of the 46-yr time series of the four-run ensemble averages for a given forcing scenario. Shown in Fig. 3 are the distributions of the difference between the normalized warm and cold composites of the precipitation for

the JJA season of year (0) [hereafter abbreviated as JJA(0); see left panels], and the DJF season six months later [i.e., December of year (0) through February of year (+1), hereafter abbreviated as DJF(0/1); see right panels]. Results are presented for the TOGA (top row), TOGA-ML (middle row), and GOGA (bottom row) experiments. We shall henceforth refer to such patterns as the ''warm minus cold'' composites. If the precipitation response is essentially linear, the charts in Fig. 3 would qualitatively correspond to the typical anomalous patterns during warm ENSO episodes; the same charts with reversed polarity would describe the typical patterns during cold ENSO episodes.

A ubiquitous feature in all six panels of Fig. 3 is the dipolar pattern in the near-equatorial western Pacific, with below-normal precipitation (during warm events) in the sector between ~120° and ~150°E, and above-normal precipitation east of ~160°E. (Note that the positive anomaly extends beyond the eastern edge of the plotting domain.) During the JJA(0) season, the most notable precipitation signals in the Northern Hemisphere are the negative anomalies over a broad region extending from the Arabian Sea across the Indian subcontinent to the Bay of Bengal, and another dry region over the subtropical western Pacific off the Chinese coast. The dry condition in the Indian summer monsoon region is particularly evident in the TOGA experiment (Fig. 3a). The corresponding anomalies simulated in the TOGA-ML and GOGA runs (Figs. 3c and 3e) have somewhat smaller spatial extents and/or weaker amplitudes. During the DJF(0/1) season (right panels of Fig. 3), all three experiments yield a positive anomaly along a belt stretching from southern Japan across southern China to the northern portion of the Indochina peninsula. This feature is seen to extend still farther southwestward to the Bay of Bengal and India in the TOGA-ML and GOGA simulations (Figs. 3d and 3f). The other noteworthy DJF(0/1) anomalies in all three experiments are the dry conditions over much of Australia and the surrounding waters, as well as over the South China Sea–Philippine Sea region.

To assess the statistical significance of the precipitation signals noted in the preceding paragraph, the Student's t-test [e.g., see Chervin and Schneider 1976, Eq. (2)] has been applied to the precipitation anomalies at individual grid points. A ''t-value'' has been obtained by dividing the difference between the warm and cold composites (presented in Fig. 3) by a measure of the variance among the eight individual warm or cold events included in the composites. The results of this analysis (not shown) indicate that, for most grid points in the Indian sector during JJA(0), as well as in southeastern Asia and northern Australia during DJF(0/1), the composite precipitation anomalies in the warm events are significantly different from those in the cold events at the 95%–99% level for the TOGA experiment. The corresponding significance levels for the TOGA-ML and GOGA experiments are typically in the ~90%–95% range.

Intercomparison among the patterns in Fig. 3 indicates that the TOGA experiment, with variable SST forcing being confined to the tropical Pacific, is capable of reproducing many features appearing in the TOGA-ML and GOGA simulations, which incorporate additional feedback processes and SST forcing sites. One could infer from this finding that these common features are primarily forced by tropical Pacific SST anomalies associated with ENSO, whereas contributions due to prescribed SST forcing or air–sea interactions at maritime sites outside of the tropical Pacific play a relatively minor role.

The model results in Fig. 3 have been evaluated using the observational estimates of the precipitation field available from the CMAP dataset (see description in section 2). This dataset covers only three warm events (1982, 1987, and 1991). Composite results for these warm ENSO years (not shown) indicate below-normal summertime rainfall in the Arabian Sea–India region and northern Australia during summer, as well as abnormally wet conditions over northern Indochina, southern China and the nearby coastal waters during winter. These observations lend some support to the simulated features in Fig. 3.

c. Interannual variability of regional precipitation indices

We shall focus our attention on the model variability in the simulated precipitation over the following monsoon regions:

- Indian subcontinent (IND) during the summer (JJA) season,
- Southeast Asia (SEA) during the winter (DJF) season, and
- Northern Australia (AUS) during the southern summer (DJF) season.

The boundaries of these regions are outlined in purple in the panels for the respective season in Fig. 3. Each region consists of ~25 contiguous land points in the model grid. At most of the grid points chosen for each region, the amplitude of the normalized warm minus cold composite anomaly in the TOGA experiment exceeds $\pm 1\sigma$. Results of the Student's t-test (see previous section) for all three regions also indicate that the local warm precipitation composites are significantly different from the corresponding cold composites.

For each of the three regions, a precipitation index for a given year was constructed by averaging the seasonally averaged anomalies over all grid points for that region, and then dividing the result by the standard deviation of the spatially averaged anomalies within the 1950–95 period. Both the anomalies and their standard deviation were computed using the four-run ensemble means for each of the SST forcing scenarios. The results

for various regions and experiments are summarized in the array of scatterplots in Fig. 4. The abscissa, in all panels of this figure, corresponds to the SST anomaly averaged over the Niño-3 region (5°S–5°N, 90°–150°W) during the appropriate season. The ordinate depicts the precipitation index for the region and experiment in question. The Niño-3 SST forcing and the associated precipitation index for a given year are indicated by a point in this coordinate system. The locations of those points for the eight warm and eight cold ENSO years are presented in the appropriate panels using colored circles and squares, respectively (see legend at bottom). The data for all other non-ENSO years in the 1950–95 period are presented using black circles. For the IND region, the scatterplot constructed using the observed all-India summer rainfall records compiled by Parthasarathy et al. (1994) for the 1950–95 period is also presented at the bottom left of Fig. 4.

The data shown in Fig. 4 clearly illustrate the negative correlations between the SST forcing in the Niño-3 region and the summertime precipitation over IND and AUS, as well as the positive correlation between the SST index and the precipitation over SEA during winter. These relationships are discernible in all three experiments examined here. Many of the ENSO years (colored circles and squares) are associated with prominent precipitation anomalies, whereas the data points for the non-ENSO years tend to cluster near the origin. The model results for the IND region are in broad agreement with the observations (see lower left panel of Fig. 4).

The linear temporal correlation coefficients between the SST anomaly in Niño-3 and various precipitation indices are displayed in the upper right corner of the individual panels in Fig. 4. The computations were performed separately for two sets of years: the first set includes all available years in the 1950–95 period, and the corresponding correlation coefficient is indicated in parentheses. The second set includes only the 16 warm/cold ENSO years, and the correlations thus obtained are shown without parentheses. All correlation coefficients shown in Fig. 4 are significant at the 99% confidence level. For most experiments and regions, the correlation values based only on the ENSO years are higher than those based on the complete dataset, thus confirming the prominent role of ENSO events in modulating the precipitation simulated in various monsoon regions. The coefficient computed using observed Indian rainfall data for the entire 1950–95 period (-0.53) falls within the range of correlation values based on the three model experiments.

The correlation between SST and Indian rainfall is somewhat lower in GOGA than in TOGA or TOGA-ML. A testing procedure using Fisher's Z transformation (Spiegel 1961) indicates that the correlation coefficient based on TOGA data for 46 summers (i.e., -0.72) is significantly different from that based on GOGA data (-0.47) at the ~94% confidence level. This result suggests that the prescription of incremental SST forcings beyond the tropical Pacific (as was done in GOGA) has the net effect of weakening the link between ENSO and Indian monsoon (as simulated in TOGA). By analyzing a 15-yr experiment similar to GOGA, Goswami (1998) has also reported a rather low correlation (-0.3) between Indian precipitation and eastern Pacific SST. The correlation coefficients between SST and precipitation indices for the SEA and AUS regions are comparable for all three experiments, thus indicating that SST changes outside the tropical Pacific do not contribute significantly to the rainfall variability in these regions.

d. Intersample and interevent variability

To gain some appreciation of the variability of the precipitation responses in the four parallel integrations for each experiment, the precipitation indices as defined in the previous section have been computed using data for each individual model run (instead of the four-run ensemble average). The precipitation anomalies for the four model runs have been normalized by a common standard deviation, which is the average of the standard deviations computed using the 46-yr time series for each of the four runs. The values of various indices based on single runs in each of the eight warm and eight cold events are shown in Fig. 5. Results for the TOGA, TOGA-ML, and GOGA experiments are indicated by circles of different colors. Open circles denote values for individual runs. Solid dots indicate averages of the data represented by the four open circles for each year and experiment. For each ENSO year in the top panels, the observational estimate of the normalized all-India summer rainfall anomaly, as reported by Parthasarathy et al. (1994), is indicated by a magenta bar. For most ENSO events, the observations presented here are similar to those compiled by Sontakke et al. (1993).

The four individual runs (see open circles in Fig. 5) for a given experiment exhibit considerable scatter from the corresponding ensemble means (solid dots). Despite these sampling fluctuations, the precipitation signals in a majority of the individual runs conform with the ENSO–monsoon relationships discerned earlier in this section on the basis of four-run averages. For most of the ENSO events, the observed all-India precipitation index lies well within the cluster of data points based on the three suites of model experiments.

e. Evolution of precipitation anomalies along the equatorial Pacific

Variations in the pattern of condensational heat sources and sinks over the tropical Pacific are known to exert strong influences on the atmospheric circulations in many parts of the globe (e.g., see Trenberth et al. 1998). We conclude this section by examining the space–time development of the simulated precipitation anomalies in the Pacific sector. In the next section, these results

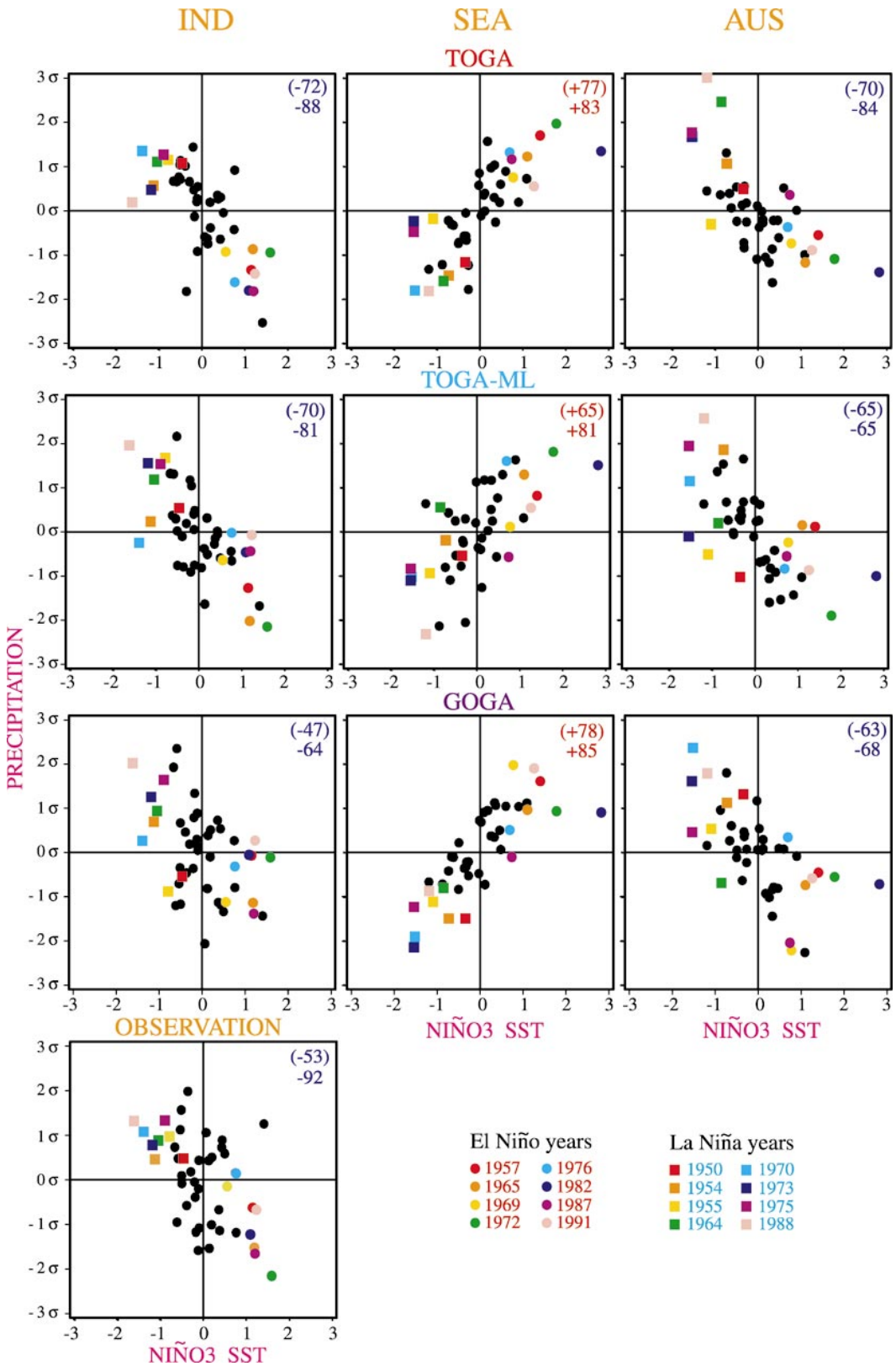

FIG. 4. Scatterplots of the area-averaged precipitation anomalies vs the prescribed SST anomalies in the Niño-3 region (5°S–5°N, 90°–150°W). The precipitation anomalies have been computed using four-run averages from TOGA (top row), TOGA-ML (second row), and GOGA (third row), and are shown for the IND region in JJA (left column),

will be used for interpreting the circulation changes over the monsoon regions during ENSO.

Shown in Fig. 6 is the time–longitude distribution of the warm minus cold composite of the tropical Pacific precipitation anomaly averaged over the latitudes between 7.8°S and 7.8°N. The composite procedure has been applied to the four-run ensemble averages of the unnormalized precipitation anomaly in the TOGA experiment for each month between March of year (0) and May of year (+1). The ENSO events are typically accompanied by a dipolelike precipitation anomaly along the equatorial Pacific. During the warm episodes, below normal rainfall is simulated in the 120°–150°E zone, whereas above-normal rainfall is generated near the date line. This dipolar pattern is well established as early as the northern summer of year (0) and persists through a period of almost an entire year thereafter.

The out-of-phase relationship between the simulated precipitation anomalies over Indonesia–New Guinea and those over the central equatorial Pacific during ENSO events is in agreement with the observational results presented by Ropelewski and Halpert (1987). This relationship is indicative of the eastward displacement of the ascending branch of the Walker circulation from the Indonesian sector to the date line during warm events, and reinforcement of the east–west contrast of the climatological precipitation field in the western and central equatorial Pacific during cold events.

5. Circulation anomalies during ENSO events

a. Model results

We now turn our attention to the atmospheric circulation features accompanying the ENSO-related precipitation anomalies described in the preceding section. Warm minus cold composites (see definition in section 4a) of the zonal and meridional wind anomalies have been constructed. The resulting streamline anomalies are displayed in Fig. 7 for the seasons of JJA(0) and DJF(0/1), and at 200 and 850 mb. The precipitation composites for the respective seasons are also shown in these patterns (see shading). All wind and precipitation data displayed in this figure are based on unnormalized four-run averages for the TOGA experiment. The corresponding composites for the TOGA-ML and GOGA experiments (not shown) are similar to those presented in Fig. 7.

1) 850 MB

The 850-mb anomalous circulation pattern in the warm phase (Figs. 7c,d) is characterized by a pair of cyclonic centers over the North and South Pacific (labeled as L_N and L_S, respectively) and another pair of anticyclonic features in the Asian–Australian–Indian Ocean sector (denoted as H_N and H_S). A notable spatial relationship exists between the cyclones/anticyclones and the dipolar precipitation pattern along the equatorial Pacific (see discussion of the latter feature in section 4e). During the northern summer (see Fig. 7c), H_N is located to the northwest of the negative precipitation anomaly over the western equatorial Pacific (indicated by minus sign), whereas L_N is situated to the northwest of the positive precipitation center over the central Pacific (denoted by plus sign). Analogously, in the southern summer (Fig. 7d), H_S (L_S) is located to the southwest (south-southeast) of the negative (positive) precipitation anomalies over the equatorial Pacific. During the winter season, the cyclones/anticyclones are displaced to the east of their respective summertime positions.

In the JJA(0) season, both anticyclones (H_N and H_S) are zonally elongated. The axes of these anomalous pressure ridges are depicted using dashed lines in Fig. 7c. The northern anticyclonic anomaly H_N is seen to be collocated with the negative precipitation anomaly in the Asian summer monsoon region (see blue shading in Fig. 7c). The wind anomaly over the latter region is oriented from the east or northeast, in opposition to the prevalent southwesterly climatological flow pattern (see Fig. 1c).

In the DJF(0/1) season (Fig. 7d), H_N is centered over the South China Sea and the Philippines, and is accompanied by below-normal precipitation. The anomalous southwesterly flow on the northern flank of H_N is directed against the climatological offshore monsoon circulation over eastern Asia during winter (see Fig. 2c), and brings about wetter than normal conditions to southern China. The reduction in strength of the northeasterly winter monsoon in the SEA region during warm ENSO events, as simulated in the TOGA experiment, is in agreement with the observational findings of Li (1990), Zhang et al. (1996), Tomita and Yasunari (1996), and W. T. Liu (1999, personal communication). The anomalous anticyclonic circulation associated with H_S leads to weakening of the climatological summer monsoon flow (see Fig. 2c) and dryness over northern Australia.

←

the SEA region in DJF (middle column), and the AUS region in DJF (right column). All precipitation anomalies have been normalized by the temporal standard deviation of the respective areal averages. In each panel, the datum for each season in the 1950–95 period is shown using either a colored circle (for selected warm ENSO years, see legend at bottom), a colored square (for cold ENSO years, see legend at bottom), or a black dot (for remaining years that do not correspond to strong ENSO events). The scatterplot based on observed all-India rainfall records for 1950–95 is shown in the bottom left. The temporal correlation coefficient (in percent) between the precipitation and SST anomalies, computed using all 45/46 data points in a given panel, is shown in parentheses at the upper right corner of the respective panel. The corresponding correlation based on only the 16 warm/cold ENSO years is shown at the upper right corner without parentheses.

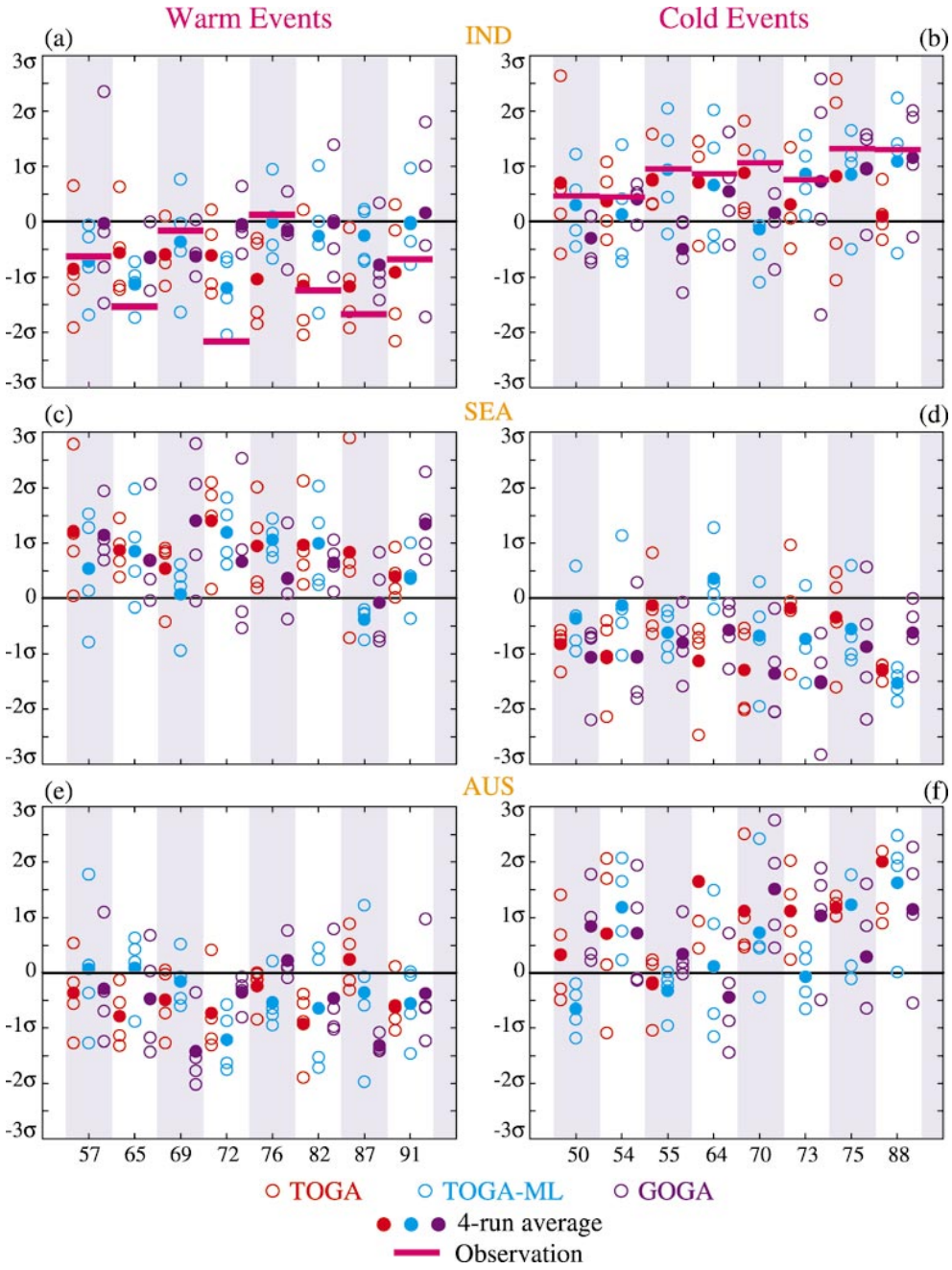

FIG. 5. Area-averaged precipitation anomalies in each of the eight selected warm (left panels) and cold (right panels) ENSO events, for the IND region in JJA (top panels), the SEA region in DJF (middle panels), and the AUS region in DJF (bottom panels). Open circles indicate the four individual runs for a given SST forcing scenario. Filled circles indicate the corresponding four-run averages. Results from the TOGA, TOGA-ML, and GOGA experiments are depicted in red, blue, and purple, respectively. The magenta bars in the top panels indicate the observed all-India summer rainfall anomalies for the selected warm and cold ENSO years. The anomalies in the individual model runs have been normalized by the average of the standard deviations of the 46-yr time series for each of the four runs.

2) 200 MB

At the 200-mb level (Figs. 7a,b), the anomalous circulation pattern over the Pacific basin is dominated by a pair of anticyclones (labeled as $\hat{H}_N$ and $\hat{H}_S$) straddling the positive equatorial precipitation anomaly. With the exception of $\hat{H}_N$ during the winter season, these anticyclonic anomalies are situated above the cyclonic features L_N and L_S at 850 mb (Figs. 7c,d). Another noteworthy feature in the upper troposphere is the cyclonic

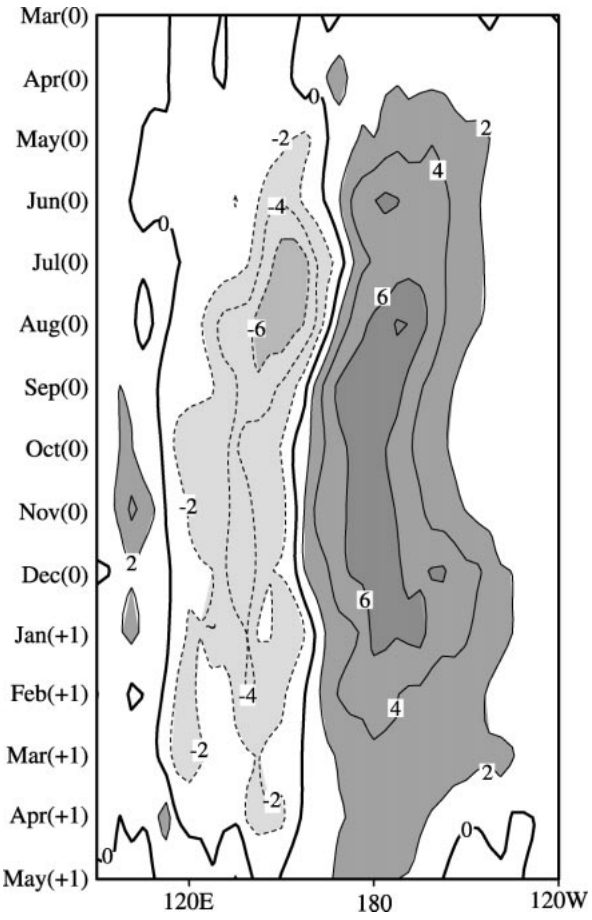

FIG. 6. Variations with time (ordinate) and longitude (abscissa) of the warm minus cold composite of precipitation anomalies simulated in the TOGA experiment. The anomalies have been averaged over the latitudes from 7.8°S to 7.8°N. Contour interval: 2 mm day^{-1}.

center $\hat{L}_N$ over eastern Asia. This center lies to the north or northwest of the negative precipitation anomaly over the subtropical western Pacific and is associated with the weakening of the climatological 200-mb Tibetan anticyclone in summer (see Fig. 1e) during warm ENSO events. The anomalous circulation pattern in Fig. 7a over the eastern Asian sector bears some resemblance to the negative phase of the observed summertime Pacific–Japan oscillation (PJO) documented by Nitta (1989). The simulated relationships between PJO, ENSO, and convective activity over the tropical western Pacific are also consistent with Nitta's observational results. Comparison between the upper and lower panels of Fig. 7 reveals a reversal in polarity of the near-equatorial zonal wind anomaly in the lower and upper troposphere, with easterlies overlying westerlies in the Pacific sector and westerlies overlying easterlies over the Indian Ocean.

3) INTERPRETATION

The placement of the cyclonic/anticyclonic centers in relation to the dipolar precipitation anomaly over the equatorial Pacific, the considerable degree of symmetry of such centers in the two hemispheres about the equator, and the baroclinic structure of the circulation anomalies, are reminiscent of the analytic solution of atmospheric responses to tropical heating, as presented by Matsuno (1966, see his Fig. 9) for a dipolelike forcing pattern, and Gill (1980, see his Fig. 1) for an isolated heat source. Specifically, the summertime anomalous anticyclone at 850 mb over southern Asia (H_N in Fig. 7c), where the monsoon rainfall is markedly reduced, may be linked to the negative diabatic heating anomaly over the western equatorial Pacific (see minus sign in Fig. 7c). In the DJF(0/1) season, the same heat sink may also play an important role in the formation of the anticyclone pair H_N and H_S (Fig. 7d), which modulate the winter monsoon over eastern Asia and the summer monsoon over northern Australia, respectively. In both Figs. 7c and 7d, the off-equatorial heat sinks over the western Pacific are collocated with equatorward wind anomalies on the eastern flank of H_N and H_S. The vorticity tendency induced by low-level divergence in these locations is thus seen to be primarily balanced by advection of planetary vorticity (i.e., the ''beta effect''). These considerations reinforce the notion that, in accord with the findings of Matsuno (1966) and Gill (1980), the anticyclonic features H_N and H_S may be partially attributed to the Rossby wave response to suppressed convective heating over the tropical western Pacific.

In summary, the model evidence presented here suggests that the ENSO events in the tropical Pacific could influence the Asian–Australian monsoon through the following chain of processes: The occurrence of warm SST anomalies in the central and eastern equatorial Pacific during El Niño events leads to an eastward displacement of the Walker circulation, resulting in anomalous sinking and diminished precipitation over the western Pacific (see Fig. 6). The reduction in condensational heating in the latter region is accompanied by the establishment of the anticyclones H_N and H_S to its northwest and southwest. These circulation anomalies oppose the climatological monsoon flows over India, Southeast Asia, and northern Australia, and they are associated with dry conditions in the IND and AUS regions during the summer season and wetness in SEA during winter.

Previously, the Matsuno–Gill theory has been invoked by Chen and Yen (1994) in linking the ENSO-related variations in tropical heating over the western Pacific to changes in the simulated monsoonal circulation over India. By analyzing the strong and weak monsoon episodes observed in the 1973–95 period, Kawamura (1998) has also noted that the Rossby wave response to fluctuations in equatorial convective heating is an important contributing factor in the coupling between ENSO and the Asian summer monsoon. The observational and modeling study of Wang et al. (2000) has provided additional evidence on the key role of ENSO cycles in modulating the low-level circulation

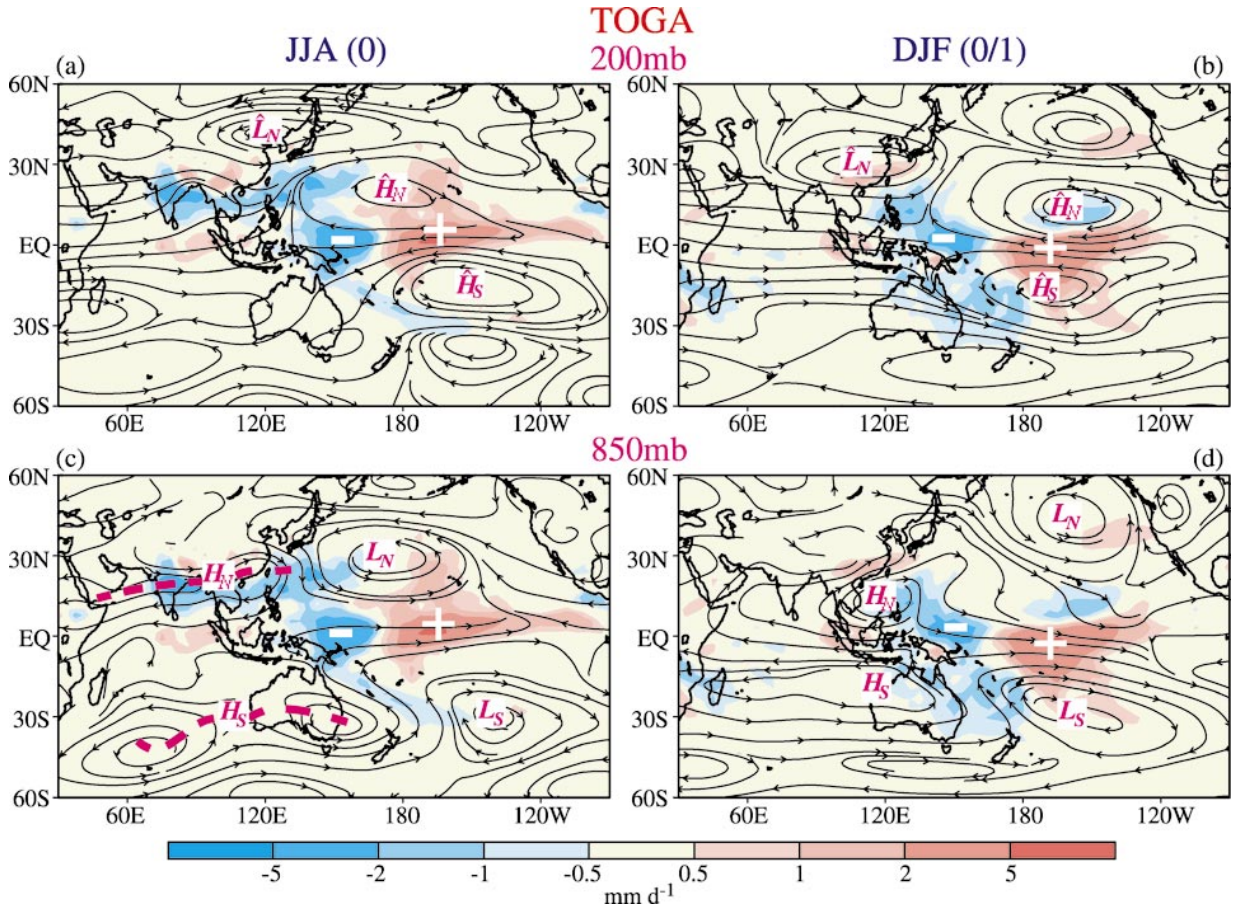

FIG. 7. Distributions of the warm minus cold composite of the anomalous streamline patterns simulated in the TOGA experiment at [(a), (b)] 200 mb and [(c), (d)] 850 mb. Results are shown for the (left panels) JJA season of year (0) and (right panels) DJF season of year (0/1). The labels L_N, L_S, H_N, and H_S denote the 850-mb cyclonic and anticyclonic centers discussed in the text. The dashed lines in (c) depict the axes of the anomalous pressure ridges associated with H_N and H_S. The circulation centers at 200 mb are indicated using similar labels with the additional overcarat symbol. The composite precipitation anomalies for the corresponding seasons are presented using shading (see scale bar at bottom; units: mm day^{-1}). Centers of positive and negative precipitation anomalies along the equatorial Pacific are indicated by plus and minus signs, respectively.

over the northwestern subtropical Pacific, thereby affecting the intensity of the eastern Asian winter monsoon. These authors further demonstrated that the anomalous wintertime anticyclone over the Philippine Sea (which corresponds closely to H_N in our Fig. 7d) during warm ENSO events is essentially a Rossby-type response to reduced condensational heating over the western equatorial Pacific. They attributed the suppressed convection in that region to subsidence forced remotely by the warm SST anomaly in the central and eastern portion of the tropical Pacific, and to local effects of the concomitant cold SST anomaly in the western portion (e.g., see Figs. 7c and 8c of Wallace et al. 1998).

b. Comparison with NCEP–NCAR reanalyses

To assess the fidelity of the horizontal and vertical structure of the circulation anomalies simulated in TOGA, we proceed to compare the model patterns with their counterparts as constructed using NCEP–NCAR reanalyses. We have highlighted the baroclinic structure of the tropical anomalies by subtracting the horizontal wind and geopotential height anomalies at 850 mb from the corresponding values at 200 mb. In view of the considerable difference in amplitude of the anomalies in the lower and upper troposphere, all data at individual pressure levels have been normalized by the local temporal standard deviations prior to the differencing procedure. The resulting streamline and geopotential thickness (see color shading) patterns are displayed in Fig. 8.

Evident in both the model and reanalysis patterns are the pair of circulation centers on both sides of the central equatorial Pacific. These features are associated with $\hat{H}_N$ and $\hat{H}_S$ at the upper level and L_N and L_S at the lower level (see Fig. 7), and are collocated with centers of positive thickness anomalies. Another pair of somewhat less distinct circulation centers with below-normal thicknesses are also discernible in the Asian–Australian

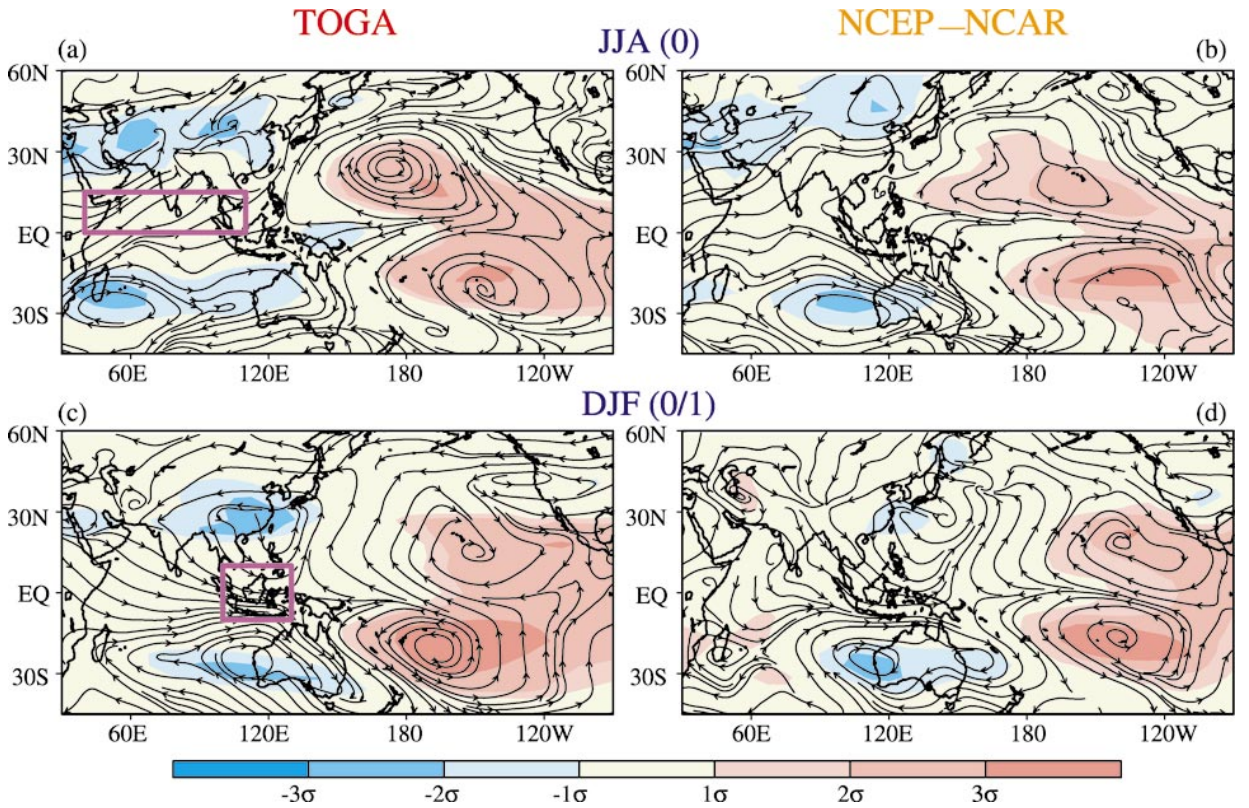

FIG. 8. As in Fig. 7, but for the streamline patterns obtained by subtracting the horizontal wind vector at 850 mb from the wind vector at 200 mb, and the thickness patterns obtained by subtracting the 850-mb height from the 200-mb height. Results are shown for the output from TOGA (left panels) and the NCEP–NCAR reanalysis data (right panels), and for the [(a), (b)] JJA season of year (0) and [(c), (d)] DJF season of year (0/1). The wind and height anomalies at individual pressure levels had been normalized by the local temporal standard deviation before differences were taken between the two levels. The purple rectangles in the left panels indicate the regions over which areal averages of zonal wind anomalies are to be computed for the construction of circulation indices.

sector in all panels of Fig. 8. These anomalies are primarily linked to H_N and H_S at 850 mb. In comparison with the Pacific sector, the lower-tropospheric flow anomalies in the Asian–Australian sector exhibit a weaker local correspondence with the circulation features at 200 mb. The polarity of these anomalies is opposite to those over the Pacific basin. Good agreement exists between model and reanalysis data with regard to the orientation of the differential flow along the equator, which is directed westward in the Pacific sector and eastward over the Indian Ocean.

c. Intersample and interevent variability

In order to illustrate the variations of the circulation responses in individuals runs and individual ENSO events for various SST forcing scenarios, further analysis has been performed on the wind data for two selected rectangular regions. The first region (see purple rectangle in Fig. 8a) is located in the near-equatorial Indian Ocean (0°–15°N, 40°–110°E). This site is characterized by strong vertical shear of the zonal wind anomalies associated with changes in the intensity of the south Asian monsoon during the JJA(0) season (see Figs. 7a and 7c, and 8a). The second domain (indicated by purple rectangle in Fig. 8c) is situated in the Indonesian sector (10°S–10°N, 100°–130°E) and serves to depict fluctuations in the zonal wind shear associated with the monsoon flows over eastern Asia and northern Australia in DJF(0/1). For each of these regions and the appropriate season, areal averages of the 200- and 850-mb zonal wind anomalies in each of the four individual runs during each of the eight warm/cold episodes have been computed. The resulting values at each pressure level were normalized by their respective temporal standard deviations, and the standardized anomalies at 850 mb were then subtracted from those at 200 mb. The standard deviation used to normalize the wind anomalies has been obtained by averaging the standard deviations of the 46-yr time series for the four individual runs. This procedure was repeated for the TOGA, TOGA-ML, and GOGA experiments. The zonal wind shear indices as defined above are similar to measures used by Webster and Yang (1992) for examining monsoon variability in the Asian–Australian region. Alternative Asian monsoon indices have also been proposed by Wang and Fan (1999) and Goswami et al. (1999).

The domain-averaged wind shear data for the selected

ENSO episodes are displayed in Fig. 9 for the Indian Ocean region in JJA(0) and for the Indonesian region in DJF(0/1). Results based on the three different SST forcing scenarios are distinguished by various colors (see legend at bottom). Indices for the four individual realizations in each scenario are plotted using open circles. Averages of these indices over the four runs are denoted by solid dots. The observational counterparts of these indices, as estimated using zonal wind data from the NCEP–NCAR reanalyses, are also shown in Fig. 9 using magenta bars.

In analogy to the precipitation anomalies shown earlier in Fig. 5, a majority of the individual runs yield the same polarity for the simulated wind shear index in a given ENSO event. By taking into account the data entries for all three experiments, 72% (88%) of the open circles in Fig. 9a (Fig. 9c) have a positive polarity (i.e., westerly anomalies overlying easterly anomalies during warm events). Conversely, 78%(86%) of the data points in Fig. 9b (Fig. 9d) are negative. In support of the model results, the wind shear indices based on the NCEP–NCAR reanalyses are mostly positive (negative) during the warm (cold) events.

6. Ocean–atmosphere coupling processes

The TOGA-ML experiment has been designed for investigating the ocean–atmosphere feedback processes in various maritime regions outside of the tropical Pacific, when the latter domain is subjected to observed SST forcing related to ENSO. We proceed to describe the nature of the air–sea coupling in the tropical Indian Ocean basin during ENSO episodes by diagnosing the mixed-layer and atmospheric responses in the TOGA-ML runs.

a. Mixed-layer response to atmospheric anomalies

Shown in Fig. 10 are the distributions of the warm minus cold composites of surface wind vector (arrows) and surface wind speed (shading) (panel a), latent heat flux (panel b), and shortwave radiative flux over south Asia and the tropical Indian Ocean (panel c). These charts are based on the four-run ensemble averages for the JJA(0) season in the TOGA-ML experiment. The values shown in Figs. 10b and 10c are taken to be positive when the flux anomaly leads to a heat gain in the oceanic mixed layer.

In the region south of ~20°N, the anomalous circulation pattern in Fig. 10a is characterized by northeasterly offshore flows over India and Indochina, and below-normal wind speeds over the Arabian Sea and the eastern portion of the Bay of Bengal.[1] The decreased wind speeds over the Arabian Sea and southeastern Bay of Bengal result in less latent heat flux from the ocean to the overlying atmosphere (or a heat gain in the mixed layer, see Fig. 10b). The negative precipitation anomalies over parts of the Arabian Sea and Bay of Bengal during warm events (see Fig. 3c) are associated with reduced cloud cover and increased solar heating of the ocean surface (Fig. 10c). The simulated variations in the cloud cover and shortwave radiation over the northern Indian Ocean during ENSO are in agreement with the observational results presented by Klein et al. (1999).

The response of the oceanic mixed layer to the above perturbations in the latent heat and radiative fluxes across the air–sea interface is illustrated in Fig. 11, which shows the warm minus cold composites of the SST as simulated in the TOGA-ML experiment during the northern summer (JJA) (panel a) and autumn (September–October–November, or SON) (panel c) of year (0). The corresponding patterns based on the observed SST field as analyzed by Smith et al. (1996) are shown in the right panels. Inspection of the left panels of Fig. 11 indicates a warming of about 0.2°C in the simulated mixed layer in the Arabian Sea and Bay of Bengal from summer to autumn of Year (0). The sites of largest temperature increases are collocated with the maxima of latent and radiative heating shown in Figs. 10b and 10c. The observational data (Figs. 11b and 11d) confirm that oceanic warming has occurred during warm ENSO events. The amplitude as well as spatial extent of the warming are larger in the observed patterns than in the model composites. The relatively weaker SST signals in the model result could partially be attributed to the assumption in the TOGA-ML experiment of a fixed mixed-layer depth of 50 m at all maritime sites. Observations [such as those compiled by Levitus (1982)] indicate that the mixed layer in much of the tropical Indian Ocean could be thinner than 50 m, thus enhancing the sensitivity of the observed ocean to fluctuations of atmospheric forcing in that region.

In an earlier observational study, Weare (1979) has similarly reported that weak summer monsoons in the Indian subcontinent are often associated with warm SST anomalies in the Arabian Sea–Indian Ocean approximately two months later. Klein et al. (1999) have also

[1] The southwesterly wind anomalies north of 20°N reinforce the climatological circulation over northern India, northern Indochina, and southern China. The line separating the northeasterly and southwesterly flows in Fig. 10a coincides with the axis of the elongated low-level anticyclone H_N appearing in the composite streamline pattern based on TOGA-ML data (not shown, similar to the TOGA result in Fig. 7c). The positive precipitation anomaly over northwestern Indochina and southwestern China during warm ENSO events (see Fig. 3c) is evidently related to the intensified southwesterly circulation in those regions.

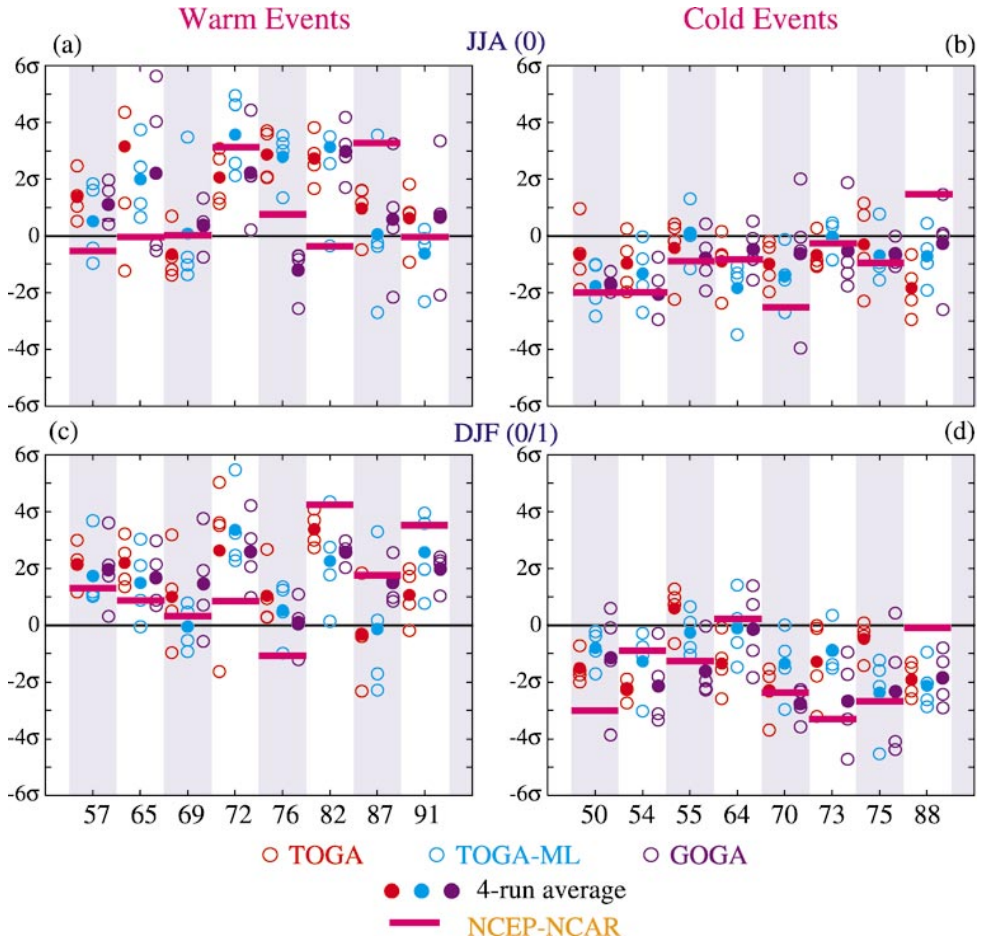

FIG. 9. As in Fig. 5, but for circulation indices obtained by subtracting area-averaged zonal wind anomalies at 850 mb from those at 200 mb, for the (upper panels) JJA season of year (0) and (lower panels) DJF season of year (0/1). The domains over which the averages have been taken correspond to the purple rectangles shown in Fig. 8a (for JJA) and Fig. 8c (for DJF). The area-averaged zonal wind anomalies for the individual runs at a given pressure level had been normalized by the averaged standard deviation over the four runs for that level before differences were taken between the two levels. The corresponding indices based on the NCEP–NCAR reanalyses are indicated using magenta bars.

noted a temporal lag of observed SST changes over the northern Indian Ocean after the onset of ENSO events.

b. Atmospheric response to mixed-layer anomalies

The TOGA-ML runs include both the ENSO-related SST forcing in the tropical Pacific and the air–sea coupling in other ocean sites, whereas the TOGA experiment has been subjected to tropical Pacific ENSO variability only, with no two-way air–sea interactions operating elsewhere. The difference between the responses in the TOGA-ML and TOGA runs would therefore provide some information on the influences of air–sea coupling outside the tropical Pacific on the model atmosphere. By the same token, the difference between the results based on the GOGA and TOGA experiments would show the atmospheric impact of observed SST anomalies prescribed outside the tropical Pacific. The warm minus cold composites of surface vector wind and precipitation for the TOGA experiment have been subtracted from the corresponding composites for the TOGA-ML experiment. The results are displayed in the left panels of Fig. 12 for the JJA(0) (panel a) and SON(0) (panel c) seasons. The analogous charts as obtained by subtracting the TOGA composites from the GOGA composites are plotted in the right panels of the same figure. Based on the arguments presented above, the patterns in Fig. 12 may be interpreted as the atmospheric responses to the positive SST anomalies in the Indian Ocean basin (see Fig. 11). These oceanic anomalies have been produced either through local air–sea interactions in TOGA-ML or by direct insertion of observational data in GOGA.

The difference charts for summer (upper panels of Fig. 12) are characterized by southwesterly surface flow over the Arabian Sea and enhanced rainfall over parts

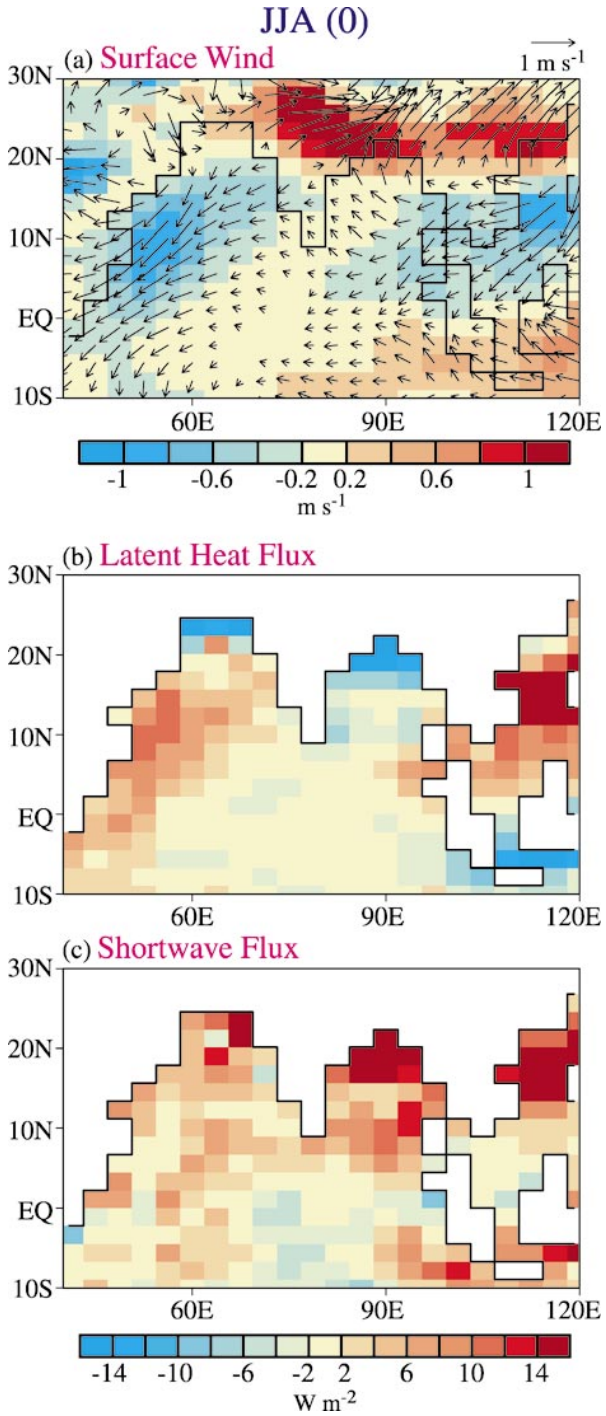

FIG. 10. Distributions of the warm minus cold composites of (a) surface wind vector (arrows; see scale at top right of panel) and wind speed (shading; see scale bar at bottom of panel; units: m s^{-1}), and fluxes of (b) latent heat and (c) shortwave radiation (see scale bar at bottom; units: W m^{-2}). All results are based on four-run averages of the TOGA-ML experiment for the JJA season of year (0). Positive (negative) values in (b) and (c) indicate heat gain (heat loss) for the oceanic mixed layer.

of India and the Bay of Bengal. The circulation and precipitation anomalies are opposite to the remote responses of these fields to the tropical Pacific ENSO forcing as simulated in the TOGA experiment (see Fig. 7c). Hence air–sea coupling in the Indian Ocean sector results in the following negative feedback loop: during warm ENSO events, the reduced intensity of the south Asian summer monsoon leads to a heat gain in the surface waters of the Arabian Sea and the Bay of Bengal through alteration of the latent heat and radiative fluxes (Fig. 10); the subsequent warming in these regions (Fig. 11) is in turn accompanied by an atmospheric circulation that enhances the strength of the monsoon in this region, thus partially offsetting the (negative) monsoon anomaly that initiated this feedback loop.

As the magnitude of the SST warming increases from summer to autumn (Fig. 11), the atmospheric responses in the latter season (lower panels of Fig. 12) are also stronger and more widespread than in summer. The southwesterly flow pattern in SON(0) extends over much of the Arabian Sea, southern India, and the Bay of Bengal, with positive precipitation changes over parts of India, the Bay of Bengal, and Indochina.

The relationship between SST fluctuations in the Indian Ocean basin and the atmospheric response as simulated in the TOGA-ML experiment may be discerned by inspection of the left panels in Figs. 11 and 12. During warm ENSO events, the SST anomaly is positive throughout much of the northern half of the Indian Ocean, and negative in the central and eastern portions of this ocean just south of the equator (Figs. 11a and 11c). The resulting basinwide meridional gradient of ocean temperature is associated with predominately anomalous northward flow near the equator (Figs. 12a and 12c), that is, from cold to warm SST anomaly. In the SON(0) season, this cross-equatorial current is seen to turn eastward in the 10°–20°N zone extending all the way from the western edge of the Arabian Sea to South China Sea. The characteristic spatial scale of this atmospheric response appears to be considerably broader than that associated with circulation anomalies that would result from changes in more local land–sea temperature contrasts, such as those between the Indian subcontinent and the Arabian Sea.

Considering the similarity between the SST changes in the northern Indian Ocean as predicted in TOGA-ML and prescribed in GOGA (Fig. 11), the difference charts based on the TOGA-ML and TOGA runs (left panels of Fig. 12) are seen to resemble those based on GOGA and TOGA (right panels). The agreement between these two sets of results demonstrates a high degree of reproducibility of the atmospheric response patterns to Indian Ocean SST anomalies.

7. Discussion

An attempt has been made in the present study to identify and understand the relationships between the

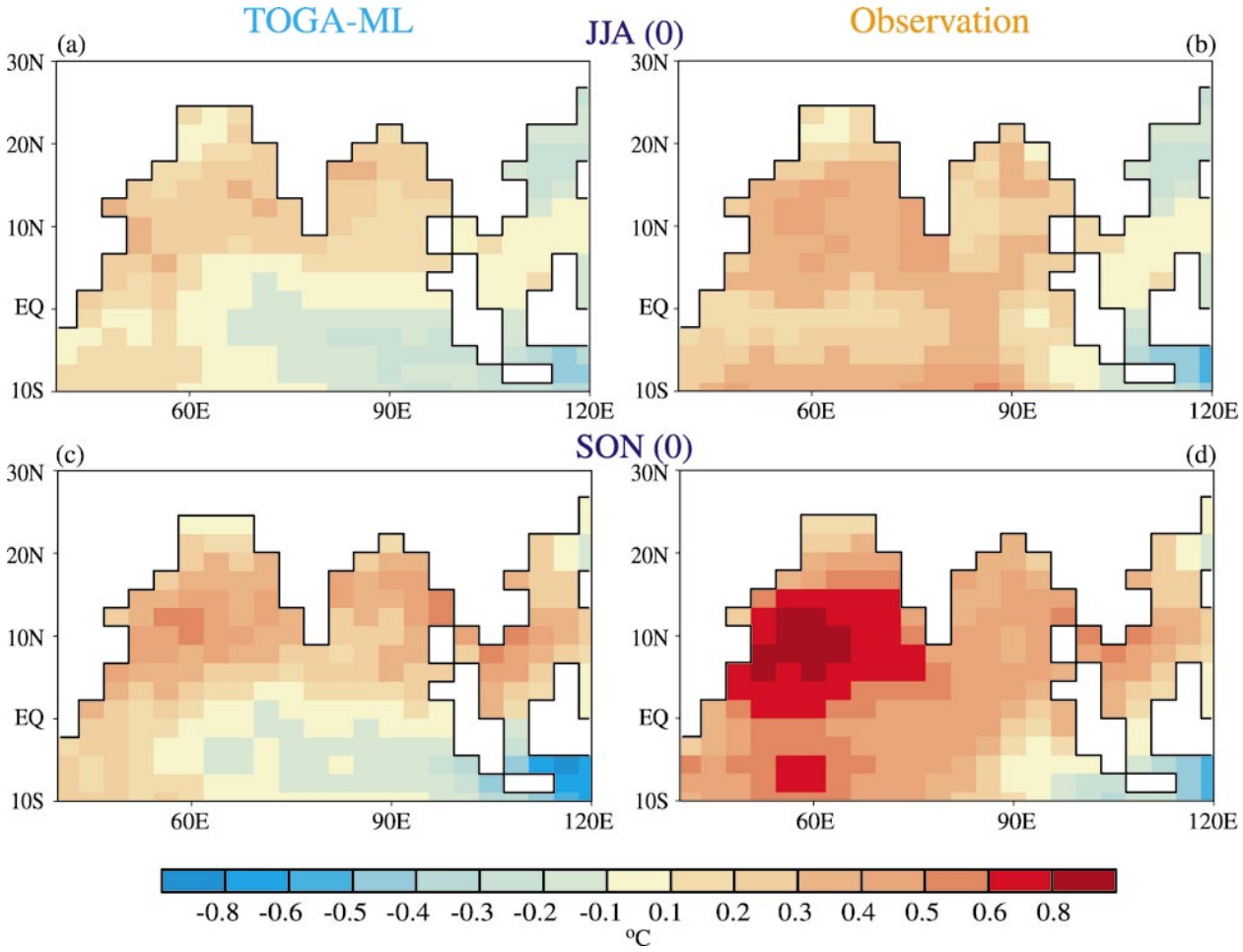

FIG. 11. Distributions of the warm minus cold composites of the sea surface temperature (shading; see scale bar at bottom; units: °C) as predicted in the TOGA-ML experiment (left panels) and as observed (right panels). Results are shown for the [(a), (b)] JJA and [(c), (d)] SON seasons of year(0).

Asian–Australian monsoons and ENSO events in the tropical Pacific. This effort has been facilitated by the availability of an extensive array of model runs that encompass different SST forcing scenarios and different ENSO events occurring in the past several decades, as well as different realizations of the model response in individual events. The large sample size generated in this suite of experiments may be appreciated by noting the multitude of raw data entries in plots such as Figs. 5 and 9. Composite analysis performed on the basis of this population of model responses yields well-defined precipitation and circulation signals in the Indian, Southeast Asian, and northern Australian sectors that are closely linked to ENSO forcing.

The circulation changes over the Asian–Australian monsoon regions during ENSO are suggestive of a Rossby wave pattern associated with a condensational heating anomaly over the western equatorial Pacific. This heating anomaly corresponds to the western portion of a dipolelike precipitation pattern. A majority of observational and modeling ENSO studies have paid more attention to the atmospheric circulation anomalies accompanying the *eastern* half of this heating complex. The evidence presented herein indicates that the *western* portion of the dipole plays a significant role in the formation of monsoon anomalies in the Asian–Australian sector. The impact of tropical western Pacific SST forcing on extratropical and monsoon variability has previously been noted by Palmer and Mansfield (1986) and Ju and Slingo (1995), respectively. The dynamical link between tropical forcing at different sites and the atmospheric flow field could be further investigated by comparing the solutions of mechanistic stationary models [such as those developed by Ting and Yu (1998)] subjected to various spatial configurations of heating anomalies in the Pacific basin. An alternative interpretation of the circulation and precipitation composites in Fig. 7 is that the streamline anomalies over the monsoon regions are linked to the in situ precipitation changes themselves. The relative importance of local versus remote heating sources in modulating the monsoonal cir-

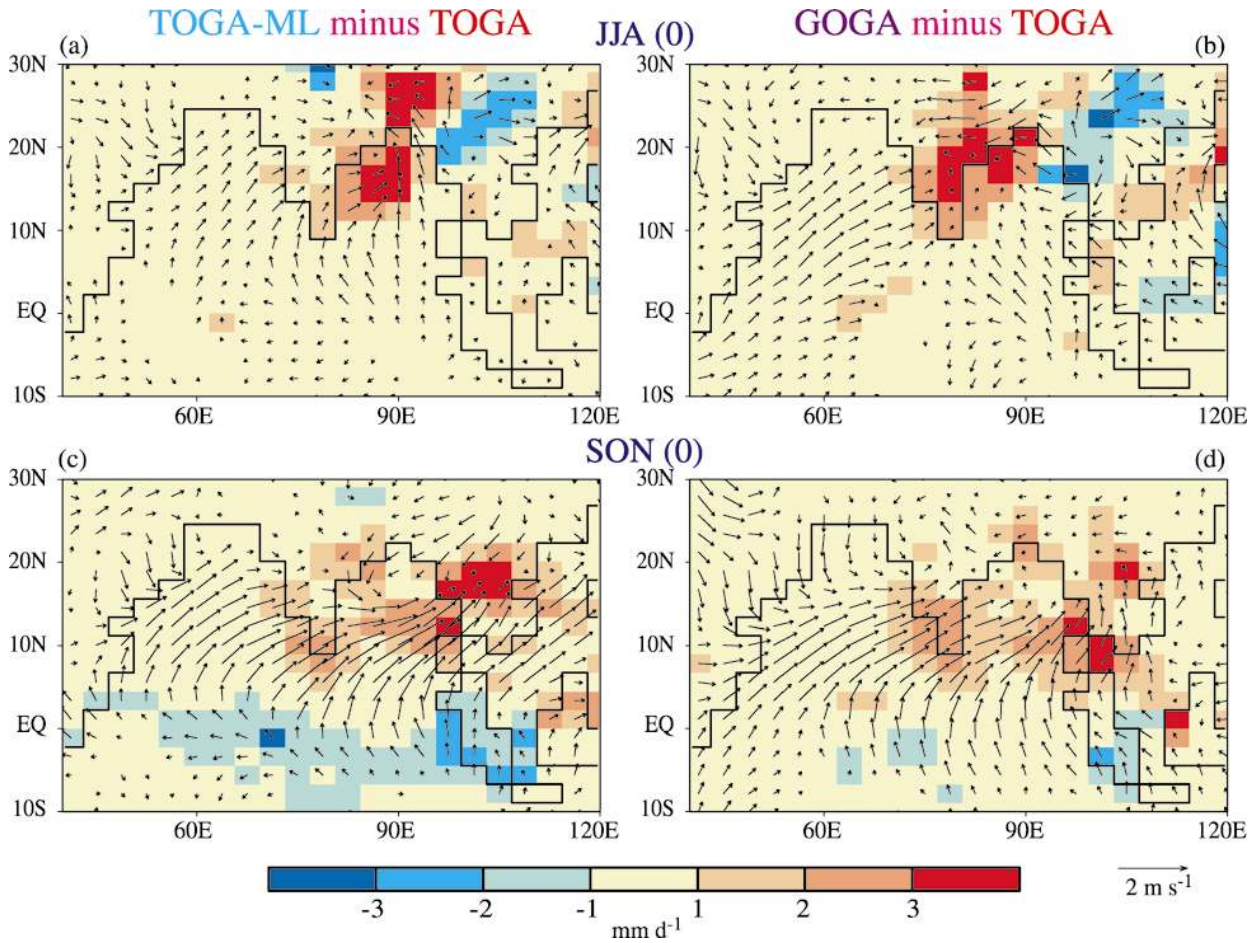

FIG. 12. Difference patterns as obtained by subtracting the warm minus cold composites for TOGA from the corresponding composites for TOGA-ML (left panels), and by subtracting the composites for TOGA from those for GOGA (right panels). Results are shown for the surface wind vector (arrows; see scale at bottom right) and precipitation (shading; see scale bar at bottom; units: mm day^{-1}) during [(a), (b)] JJA and [(c), (d)] SON of year (0).

culation could also be addressed by designing appropriate experiments with stationary models.

The evidence presented in section 6 indicates that variations in the atmospheric circulation and cloud cover over south Asia during ENSO events could induce notable changes in the surface conditions of the Indian Ocean. The processes contributing to covariability of the SST field in the tropical Pacific and Indian Ocean basins are analogous to those associated with the ''atmospheric bridge'' linking tropical ENSO episodes to SST anomalies in the extratropical oceans (e.g., see Lau and Nath 1996). By contrasting the results from model runs with and without air–sea coupling in the Indian Ocean (see Fig. 12), we further note that the Indian Ocean SST perturbations arising from ENSO-related monsoon anomalies could in turn lead to atmospheric changes that oppose such monsoon anomalies. The effects of this negative feedback loop may partially account for the somewhat weaker Indian monsoon signals (e.g., Figs. 3 and 4) in GOGA (which incorporate SST changes in the Indian Ocean) than those in TOGA (with fixed Indian Ocean SST). This same explanation may be offered for the feeble ENSO–monsoon relationship reported by Goswami (1998) on the basis of an earlier GFDL experiment similar to GOGA. The possible presence of this negative feedback in the real coupled system may also contribute to a smaller correlation coefficient between ENSO indices and observed Indian monsoon anomalies [with typical absolute amplitudes of 0.4–0.6; e.g., see Pant and Parthasarathy (1981), Shukla and Paolino (1983), and bottom left panel of our Fig. 4] as compared to the corresponding TOGA result (~0.7, see upper left panel of Fig. 4).

Further study is needed to understand the nature of the feedback mechanisms associated with air–sea interactions in the monsoon regions. The atmospheric response to Indian Ocean SST anomalies, as inferred indirectly from differences between the TOGA-ML and TOGA runs (Fig. 12), needs to be substantiated by additional experiments with GCMs and simplified stationary models subjected to SST forcing in the Indian Ocean, such as that shown in Fig. 11. The model di-

agnostics described in section 6 suggest that interesting lag relationships exist between the atmospheric forcing due to the monsoon anomalies (Fig. 10) in JJA(0), the resulting SST changes [which attain maximum amplitudes in SON(0), see Fig. 11], and the atmospheric responses to such changes [which are also strongest in SON(0), see Fig. 12]. The approximately one-season delay of the atmospheric feedback signal reduces somewhat the impact of this negative feedback mechanism on the intensity of the Indian monsoon during the peak summer season. These model findings on the seasonal dependence of, and temporal lags between, variations in different components of the coupled system need to be checked against observational data.

For the cold season, the important role of thermodynamic air–sea interaction in maintaining the near-surface anticyclonic anomaly over the Philippine Sea (e.g., see H_N in Fig. 7d) and the local sea surface cooling during warm ENSO events has been pointed out by Wang et al. (2000). These authors further noted that such atmospheric and oceanic anomalies in the western tropical Pacific could persist through the following spring, thus affecting the rainfall amounts along the east Asian subtropical frontal zone during the Mei-yu season.

The role of the atmospheric bridge in forcing SST changes in ocean sites lying outside of the tropical Pacific also has important implications on the design and interpretation of GCM experiments for studying the origin of atmospheric and oceanic variability. For instance, prescription of observed Indian Ocean SST anomalies as the lower boundary condition for atmospheric GCM integrations (as is done in the GOGA experiment) may not capture the essence of air–sea coupling in that region, since these SST anomalies could in part arise from atmospheric forcing. Kumar and Hoerling (1998) have raised similar concerns while examining output from model runs subjected to prescribed SST forcing in the Indian Ocean.

Warm and cold composites of various indicators of land surface processes (e.g., land surface temperature, soil moisture, and snow depth) have been constructed for individual seasons. The results (not shown) for the period from December of year (−1) through May of year (0) do not indicate any organized and large-scale signals in the Eurasian landmass. Hence the land processes in winter and spring do not seem to play a substantial role in the subsequent development of ENSO-related variations of the south Asian summer monsoon. Modeling studies by Lau and Bua (1998), Goswami (1998), and Yang and Lau (1998) have similarly reported that the impact of SST anomalies on large-scale interannual monsoon variability is stronger than that of air–land interactions. On the other hand, the composites for the JJA(0) season reveal that the weak (strong) monsoon anomalies during warm (cold) ENSO events are typically accompanied by noticeable land surface warming (cooling) over the Indian subcontinent. These temperature anomalies tend to persist through the following autumn and winter. The resulting changes in the land–sea contrast could in turn influence the monsoon circulation. This air–land coupling process is analogous to the air–sea feedbacks over the Indian Ocean, as described in section 6.

This study is focused on the influences of ENSO-related processes on monsoon variability. Many other factors (such as those mentioned in the introduction) probably also contribute to the monsoon anomalies in the observed and model atmospheres. While we have reported some success in identifying the ENSO–monsoon relationships by aggregating the ensemble model responses over many events, considerable scatter of the model signals exists from event to event, and from one member of the ensemble to another (see Figs. 4, 5, and 9). A better understanding of the specific roles of different processes in such interevent and intersample fluctuations would advance our skill in performing forecasts for the monsoon regions.

Acknowledgments. We thank A. J. Broccoli, B. N. Goswami, I. M. Held, S. A. Klein, J. R. Lanzante, W. F. Stern, B. Wang, S. Yang, and three official reviewers for offering constructive comments on a preliminary version of this manuscript; W. T. Liu for sharing with us the ENSO composite results based on ship observations; and J. J. Ploshay and B. J. Soden for assistance with accessing the NCEP–NCAR and CMAP datasets, respectively. The NCEP–NCAR reanalyses have been obtained from NCEP (see its Web site at http://wesley.wwb.noaa.gov/reanalysis.html for further details). The CMAP dataset has been archived at the Data Support Section of NCAR. This study is part of a NOAA/Universities collaborative effort for model diagnosis, which is supported by the Climate and Global Change Program of NOAA.

REFERENCES

Alexander, M. A., and J. D. Scott, 1995: *Atlas of Climatology and Variability in the GFDL R30S14 GCM.* CIRES, University of Colorado, 121 pp. [Available from the authors at CDC/NOAA, R/E/CD1, 325 Broadway, Boulder, CO 80303-3328.]

Angell, J. K., 1981: Comparison of variations in atmospheric quantities with sea surface temperature variations in the equatorial eastern Pacific. *Mon. Wea. Rev.,* **109,** 230–243.

Arpe, K., L. Dümenil, and M. A. Giorgetta, 1998: Variability of the Indian monsoon in the ECHAM3 Model: Sensitivity to sea surface temperature, soil moisture, and the stratospheric quasi-biennial oscillation. *J. Climate,* **11,** 1837–1858.

Barnett, T. P., L. Dümenil, U. Schlese, E. Roekler, and M. Latif, 1989: The effect of Eurasian snow cover on regional and global climate variations. *J. Atmos. Sci.,* **46,** 661–685.

Broccoli, A. J., and S. Manabe, 1992: The effects of orography on midlatitude Northern Hemisphere dry climates. *J. Climate,* **5,** 1181–1201.

Chang, C.-P., Y. Zhang, and T. Li, 2000a: Interannual and interdecadal variations of the East Asian summer monsoon and tropical Pacific SSTs. Part I: Roles of the subtropical ridge. *J. Climate,* **13,** 4310–4325.

——, ——, and ——, 2000b: Interannual and interdecadal variations

of the East Asian summer monsoon and tropical Pacific SSTs. Part II: Meridional structure of the monsoon. *J. Climate,* **13,** 4326–4340.

Chen, T.-C., and M.-C. Yen, 1994: Interannual variation of the Indian monsoon simulated by the NCAR Community Climate Model: Effect of the tropical Pacific SST. *J. Climate,* **7,** 1403–1415.

Chervin, R. M., and S. H. Schneider, 1976: On determining the statistical significance of climate experiments with general circulation models. *J. Atmos. Sci.,* **33,** 405–412.

Drosdowsky, W., and M. Williams, 1991: The Southern Oscillation in the Australian region. Part I: Anomalies at the extremes of the oscillation. *J. Climate,* **4,** 619–638.

Gates, W. L., 1992: AMIP: The Atmospheric Model Intercomparison Project. *Bull. Amer. Meteor. Soc.,* **73,** 1962–1970.

Gill, A. E., 1980: Some simple solutions for heat-induced tropical circulation. *Quart. J. Roy. Meteor. Soc.,* **106,** 447–462.

Gordon, C. T., and W. F. Stern, 1982: A description of the GFDL global spectral model. *Mon. Wea. Rev.,* **110,** 625–644.

Goswami, B. N., 1998: Interannual variations of Indian summer monsoon in a GCM: External conditions versus internal feedbacks. *J. Climate,* **11,** 501–522.

——, V. Krishnamurthy, and H. Annamalai, 1999: A broad-scale circulation index for the interannual variability of the Indian summer monsoon. *Quart. J. Roy. Meteor. Soc.,* **125,** 611–633.

Ju, J., and J. Slingo, 1995: The Asian summer monsoon and ENSO. *Quart. J. Roy. Meteor. Soc.,* **121,** 1133–1168.

Kalnay, E., and Coauthors, 1996: The NCEP/NCAR 40-Year Reanalysis Project. *Bull. Amer. Meteor. Soc.,* **77,** 437–471.

Kawamura, R., 1998: A possible mechanism of the Asian summer monsoon–ENSO coupling. *J. Meteor. Soc. Japan,* **76,** 1009–1027.

Kitoh, A., 1992: Simulated interannual variations of the Indo-Australian monsoons. *J. Meteor. Soc. Japan,* **70,** 563–583.

Klein, S. A., B. J. Soden, and N.-C. Lau, 1999: Remote sea surface temperature variations during ENSO: Evidence for a tropical atmospheric bridge. *J. Climate,* **12,** 917–932.

Krishna Kumar, K., B. Rajagopalan, and M. A. Cane, 1999: On the weakening relationship between the Indian monsoon and ENSO. *Science,* **284,** 2156–2159.

Kumar, A., and M. P. Hoerling, 1998: Specification of regional sea surface temperatures in atmospheric general circulation model simulations. *J. Geophys. Res.,* **103,** 8901–8907.

Lau, K.-M., and W. Bua, 1998: Mechanisms of monsoon–Southern Oscillation coupling: Insights from GCM experiments. *Climate Dyn.,* **14,** 759–779.

Lau, N.-C., and M. J. Nath, 1994: A modeling study of the relative roles of tropical and extratropical SST anomalies in the variability of the global atmosphere–ocean system. *J. Climate,* **7,** 1184–1207.

——, and ——, 1996: The role of the atmospheric bridge in linking tropical Pacific ENSO events to extratropical SST anomalies. *J. Climate,* **9,** 2036–2057.

Levitus, S., 1982: *Climatological Atlas of the World Ocean.* NOAA Professional Paper 13, 173 pp.

Li, C., 1990: Interaction between anomalous winter monsoon in East Asia and El Niño events. *Adv. Atmos. Sci.,* **7,** 36–46.

Lindberg, C., and A. J. Broccoli, 1996: Representation of topography in spectral climate models and its effect on simulated precipitation. *J. Climate,* **9,** 2641–2659.

Matsuno, T., 1966: Quasi-geostrophic motions in the equatorial area. *J. Meteor. Soc. Japan,* **44,** 25–43.

McBride, J. L., and N. Nicholls, 1983: Seasonal relationships between Australian rainfall and the Southern Oscillation. *Mon. Wea. Rev.,* **111,** 1998–2004.

Meehl, G. A., 1994: Coupled ocean–atmosphere–land processes and south Asian monsoon variability. *Science,* **265,** 263–267.

——, and J. M. Arblaster, 1998: The Asian–Australian monsoon and El Niño–Southern Oscillation in the NCAR Climate System Model. *J. Climate,* **11,** 1356–1385.

Mooley, D. A., and B. Parthasarathy, 1983: Indian summer monsoon and El Niño. *Pure Appl. Geophys.,* **121,** 339–352.

Nitta, T., 1989: Global features of the Pacific–Japan oscillation. *Meteor. Atmos. Phys.,* **41,** 5–12.

Normand, C., 1953: Monsoon seasonal forecasting. *Quart. J. Roy. Meteor. Soc.,* **79,** 463–473.

Palmer, T. N., and D. A. Mansfield, 1986: A study of wintertime circulation anomalies during past El Niño events using a high resolution general circulation model. II: Variability of the seasonal mean response. *Quart. J. Roy. Meteor. Soc.,* **112,** 639–660.

——, C. Brankovic, P. Viterbo, and M. J. Miller, 1992: Modeling interannual variations of summer monsoons. *J. Climate,* **5,** 399–417.

Pant, G. B., and B. Parthasarathy, 1981: Some aspects of an association between the Southern Oscillation and Indian summer monsoon. *Arch. Meteor. Geophys. Bioklimatol.,* **B29,** 245–252.

Parthasarathy, B., A. A. Munot, and D. R. Kothawale, 1994: All-Indian monthly and seasonal rainfall series: 1871–1993. *Theor. Appl. Climatol.,* **49,** 217–224.

Rasmusson, E. M., and T. H. Carpenter, 1983: The relationship between the eastern Pacific sea surface temperature and rainfall over India and Sri Lanka. *Mon. Wea. Rev.,* **111,** 517–528.

Ropelewski, C. F., and M. S. Halpert, 1987: Global and regional scale precipitation patterns associated with the El Niño/Southern Oscillation. *Mon. Wea. Rev.,* **115,** 1606–1626.

——, and ——, 1989: Precipitation patterns associated with the high index phase of the Southern Oscillation. *J. Climate,* **2,** 268–284.

Sankar-Rao, M., K.-M. Lau, and S. Yang, 1996: On the relationship between Eurasian snow cover and the Asian summer monsoon. *Int. J. Climatol.,* **16,** 605–616.

Shukla, J., and D. A. Paolino, 1983: The Southern Oscillation and long range forecasting of the summer monsoon rainfall over India. *Mon. Wea. Rev.,* **111,** 1830–1837.

Smith, T. M., R. W. Reynolds, R. E. Livezey, and D. C. Stokes, 1996: Reconstruction of historical sea surface temperatures using empirical orthogonal functions. *J. Climate,* **9,** 1403–1420.

Soman, M. K., and J. Slingo, 1997: Sensitivity of the Asian summer monsoon to aspects of sea-surface-temperature anomalies in the tropical Pacific Ocean. *Quart. J. Roy. Meteor. Soc.,* **123,** 309–336.

Sontakke, N. A., G. B. Pant, and N. Singe, 1993: Construction of all-India summer monsoon rainfall series for the period 1844–1991. *J. Climate,* **6,** 1807–1811.

Sperber, K. R., and T. N. Palmer, 1996: Interannual tropical rainfall variability in general circulation model simulations associated with the Atmospheric Model Intercomparison Project. *J. Climate,* **9,** 2727–2750.

Spiegel, M. R., 1961: *Schaum's Outline of Theory and Problems of Statistics.* Schaum Publishing Company, 359 pp.

Ting, M., and L. Yu, 1998: Steady response to tropical heating in wavy linear and nonlinear baroclinic models. *J. Atmos. Sci.,* **55,** 3565–3582.

Tomita, T., and T. Yasunari, 1996: Role of the northeast winter monsoon on the biennial oscillation of the ENSO/monsoon system. *J. Meteor. Soc. Japan,* **74,** 399–413.

Trenberth, K. E., 1997: The definition of El Niño. *Bull. Amer. Meteor. Soc.,* **78,** 2771–2777.

——, G. W. Branstator, D. Karoly, A. Kumar, N.-C. Lau, and C. Ropelewski, 1998: Progress during TOGA in understanding and modeling global teleconnections associated with tropical sea surface temperatures. *J. Geophys. Res.,* **103,** 14 291–14 324.

Troup, A. J., 1965: The Southern Oscillation. *Quart. J. Roy. Meteor. Soc.,* **91,** 490–506.

Walker, G. T., 1923: Correlation in seasonal variations of weather. III: A preliminary study of world weather. *Mem. Indian Meteor. Dept.,* **24,** 75–131.

——, 1924: Correlation in seasonal variations of weather. IV: A further study of world weather. *Mem. Indian Meteor. Dept.,* **24,** 275–332.

Wallace, J. M., E. M. Rasmusson, T. P. Mitchell, V. E. Kousky, E. S. Sarachik, and H. von Storch, 1998: On the structure and evolution of ENSO-related climate variability in the tropical Pacific: Lessons from TOGA. *J. Geophys. Res.,* **103,** 14 241–14 259.

Wang, B., and Z. Fan, 1999: Choice of South Asian summer monsoon indices. *Bull. Amer. Meteor. Soc.,* **80,** 629–638.

——, R. Wu, and X. Fu, 2000: Pacific–East Asian teleconnection: How does ENSO affect East Asian climate? *J. Climate,* **13,** 1517–1536.

Weare, B. C., 1979: A statistical study of the relationships between ocean surface temperatures and the Indian monsoon. *J. Atmos. Sci.,* **36,** 2279–2291.

Webster, P. J., and S. Yang, 1992: Monsoon and ENSO: Selectively interactive systems. *Quart. J. Roy. Meteor. Soc.,* **118,** 877–926.

——, V. O. Magaña, T. N. Palmer, J. Shukla, R. A. Tomas, M. Yanai, and T. Yasunari, 1998: Monsoons: Processes, predictability, and the prospects for prediction. *J. Geophys. Res.,* **103,** 14 451–14 510.

Xie, P., and P. A. Arkin, 1997: Global precipitation: A 17-year monthly analysis based on gauge observations, satellite estimates, and numerical model outputs. *Bull. Amer. Meteor. Soc.,* **78,** 2539–2558.

Yang, S., and K.-M. Lau, 1998: Influences of sea surface temperature and ground wetness on Asian summer monsoon. *J. Climate,* **11,** 3230–3246.

Yasunari, T., 1989: A possible link of QBOs between the stratosphere, troposphere and sea surface temperature in the tropics. *J. Meteor. Soc. Japan,* **67,** 483–493.

Zhang, R., A. Sumi, and M. Kimoto, 1996: Impact of El Niño on the east Asian monsoon: A diagnostic study of the ’86/87 and ’91/92 events. *J. Meteor. Soc. Japan,* **74,** 49–62.